# Chapter 3

# Development of Solutal Marangoni convection in V-shaped containers: a model

## 3.1    Introduction

In chapter 2, microgravity experiments in V-shaped containers were described. In this chapter, the flow and the concentration distribution in these V-shaped containers are modelled numerically. The computations are limited to a flat container and to a convex container. The experiments corresponding to these computations are the experiments with containers 1 and 5 (flat containers) and the containers 2, 4, and 7 (convex containers). Since the experiments with containers 4, 5 and 7 were most successful, the results obtained for these containers are referred to when the results of the computations are discussed.

Firstly, the geometry and the equations used in the computations are described. Then the numerical method is outlined. Finally, the results are presented and discussed for the flat container as well as the convex container.

## 3.2    Description of the systems

Calculations on similar systems have been performed in the past [1] by Hoogstraten et al. In their paper, only the liquid phase was taken into account, and an Alternate Direction Implicit (A.D.I.) scheme was used to solve the Navier-Stokes equation, the continuity equation, and the convection-diffusion equation simultaneously. However, due to coupling of the various equations through the boundary conditions, the numerical scheme was not entirely implicit and their whole method suffered from the necessity to use very small time steps to obtain a stable solution. Actually, calculations in their paper were not carried out beyond 1.25 second, which is too short compared to the experimental time scale. These considerations are discussed in more detail in section 3.3.

After updating and analysing the routines used by Hoogstraten et al. [1], it was concluded that a different numerical method had to be used, which could solve the system of equations simultaneously and implicitly for each time step. Furthermore, after analysing the first results of this method and the results of the previous method, it was established that the gas phase had to be taken into account to get an accurate description of the experimental results. A more detailed discussion of this result is presented in section 3.4.

In the remainder of this chapter, only the system is described that was actually used in the final computations. This system is two-dimensional, since it was not believed that a third dimension would provide a completely different picture and it would certainly increase memory

and time requirements for the computations. The system consists of a liquid phase and a gas phase, in much the same fashion as used in the experiments. The liquid contains 5 wt % acetone and the acetone evaporates from the liquid to the gas phase. The Marangoni effect sets liquid as well as gas in motion. The gas phase is supposed not to be disturbed by any flow outside the experimental system. Two different containers with respect to geometry have been used in the computations and they are now described separately.

*Flat container*

The geometry used for the flat container is sketched in figure 1. The liquid phase is triangular and contained by two solid walls. At $y = H_L$ the liquid-air interface is present. The air phase is contained by two solid walls inclined at 45 ° and a solid no-slip wall at the top. The wall at the top is permeable to acetone. A Cartesian x-y co-ordinate system is adopted. Velocities in x- and y-direction are denoted as u and v respectively.
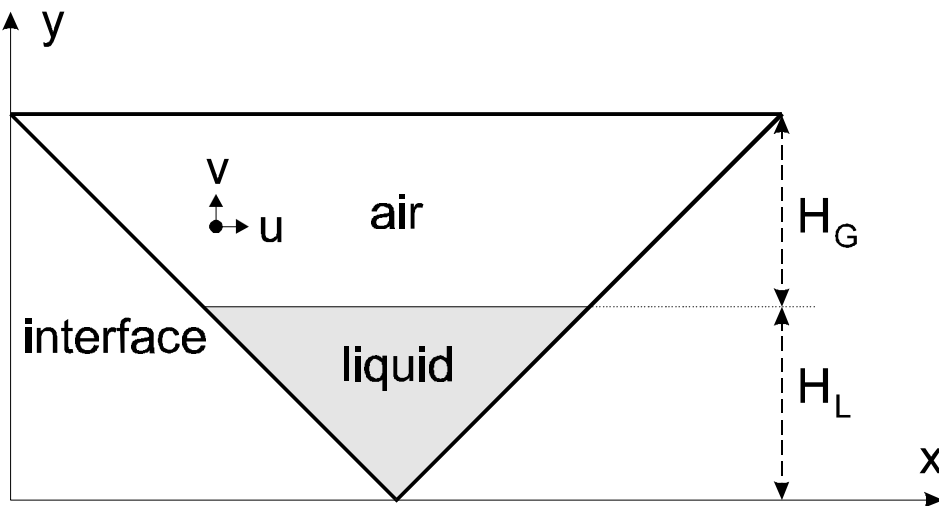


figure 1      *The geometry in case of a flat container. In the experimental case $H_L = H_G$*
              *= 0.0141 m.*

Firstly, the stream function $\psi$ and the vorticity $\omega$ are introduced:

$$u = -\frac{\partial \psi}{\partial y} \tag{1}$$

$$v = \frac{\partial \psi}{\partial x} \tag{2}$$

$$\omega = \frac{\partial u}{\partial y} - \frac{\partial v}{\partial x} \tag{3}$$

The equations describing the transport of mass and momentum in this geometry are the Navier-Stokes equation, the continuity equation and the convection-diffusion equation. The liquid is assumed to be Newtonian and incompressible and the diffusive mass transport can be described by the Fick law, because acetone concentrations are low. The governing equation for stream function, vorticity and concentration c can be written as:

$$\frac{\partial \omega}{\partial t} - \frac{\partial \psi}{\partial y}\frac{\partial \omega}{\partial x} + \frac{\partial \psi}{\partial x}\frac{\partial \omega}{\partial y} = \nu_P \nabla^2 \omega \tag{4}$$

$$\omega = -\nabla^2 \psi \tag{5}$$

$$\frac{\partial c}{\partial t} - \frac{\partial \psi}{\partial y}\frac{\partial c}{\partial x} + \frac{\partial \psi}{\partial x}\frac{\partial c}{\partial y} = D_P \nabla^2 c \tag{6}$$

In these equations, $\nu_P$ and $D_P$ are the kinematic viscosity and the solute diffusion coefficient in the phase P (liquid (L) or gas (G)) under consideration, t is time and $\nabla^2$ is the two-dimensional Laplacian operator.

At the solid boundaries, the following boundary conditions apply:

$$\psi = 0 \tag{7}$$

$$\mathbf{n} \cdot \nabla \psi = 0 \tag{8}$$

$$\mathbf{n} \cdot \nabla c = 0 \qquad \text{(left and right wall)} \tag{9}$$

$$c = 0 \qquad \text{(permeable top wall)} \tag{10}$$

In these equations, $\mathbf{n}$ is the normal vector to the boundary. For the liquid-gas interface, the following assumptions are supposed to hold:

- There is local thermodynamic equilibrium (equation 12).
- No accumulation of mass takes place at the interface (equation 13).
- The interface behaves Newtonian and the surface viscosity coefficients are negligible (equation 14).
- The interface does not deform (equation 15).
- There is no slip at the interface (equation 16).

These assumptions result in the following boundary conditions at the liquid-gas interface:

$$\psi = 0 \tag{11}$$

$$c_{i,G} = m\, c_{i,L} \tag{12}$$

$$D_L\left(\mathbf{n} \cdot \nabla c_L\right) = D_G\left(\mathbf{n} \cdot \nabla c_G\right) \tag{13}$$

$$\left(\frac{d\gamma}{dc}\right)\nabla_\Gamma \cdot c_L = \mu_L\left(-\frac{\partial^2 \psi}{\partial y^2}\right)_L - \mu_G\left(-\frac{\partial^2 \psi}{\partial y^2}\right)_G \tag{14}$$

$$\nabla_\Gamma^2 \cdot \psi = 0 \tag{15}$$

$$u_L = u_G \Leftrightarrow \left(\frac{\partial \psi}{\partial y}\right)_L = \left(\frac{\partial \psi}{\partial y}\right)_G \tag{16}$$

In these equations, the subscript i refers to the interface, and $\nabla_\Gamma$ and $\nabla_\Gamma^2$ are the nabla and the Laplacian operator parallel to the interface. These equations are non-dimensionalised by scaling distance, time, stream function, vorticity, concentration in the liquid and concentration in the gas phase by $H_L$, $H_L^2/\nu_L$, $\nu_L$, $\nu_L/H_L^2$, $c_0$ (initial liquid concentration) and $m \cdot c_0$, respectively.

From now on, concentration (c), stream function ($\psi$) and vorticity ($\omega$) are dimensionless quantities. The set of dimensionless equations and boundary conditions now read (dimensionless equations that are identical to the dimensional equations are not repeated):

$$\frac{\partial \omega}{\partial t} - \frac{\partial \psi}{\partial y}\frac{\partial \omega}{\partial x} + \frac{\partial \psi}{\partial x}\frac{\partial \omega}{\partial y} = Vi_P \left(\frac{\partial^2 \omega}{\partial x^2} + \frac{\partial^2 \omega}{\partial y^2}\right) \tag{17}$$

$$\frac{\partial c}{\partial t} - \frac{\partial \psi}{\partial y}\frac{\partial c}{\partial x} + \frac{\partial \psi}{\partial x}\frac{\partial c}{\partial y} = \frac{Vi_P}{Sc_P} \left(\frac{\partial^2 c}{\partial x^2} + \frac{\partial^2 c}{\partial y^2}\right) \tag{18}$$

$$c_{i,G} = c_{i,L} \tag{19}$$

$$\left.\frac{\partial c}{\partial y}\right|_L = Bi_N \left.\frac{\partial c}{\partial y}\right|_G \tag{20}$$

$$\omega_L - \frac{\mu_G}{\mu_L}\omega_G = -\frac{Ma}{Sc_L}\frac{\partial c}{\partial x} \tag{21}$$

The dimensionless numbers appearing in the equations are the Marangoni number, a Biot number $Bi_N$, the liquid and the gas phase Schmidt numbers, and the viscosity ratio $Vi_P$. Note that the Biot number $Bi_N$ is not defined as the mass transfer resistance ratio, as it usually is. Therefore, this Biot number is referred to as the numerical Biot number.

$$Ma = \frac{\left(-\frac{d\gamma}{dc}\right)c_0 H_L}{\mu_L D_L} \tag{22}$$

$$Bi_N = m \cdot \frac{D_G}{D_L} \tag{23}$$

$$Sc_P = \frac{\nu_P}{D_P} \tag{24}$$

$$Vi_P = \frac{\nu_P}{\nu_L} \tag{25}$$

*Convex container*

The geometry used for this case is sketched in figure 2. A cylindrical co-ordinate system is employed. Velocities in r and θ-direction are denoted $v_r$ and $v_\theta$, respectively. The angle between the solid walls is an integer multiple of π/4. The integer multiple is denoted by $N_P$.
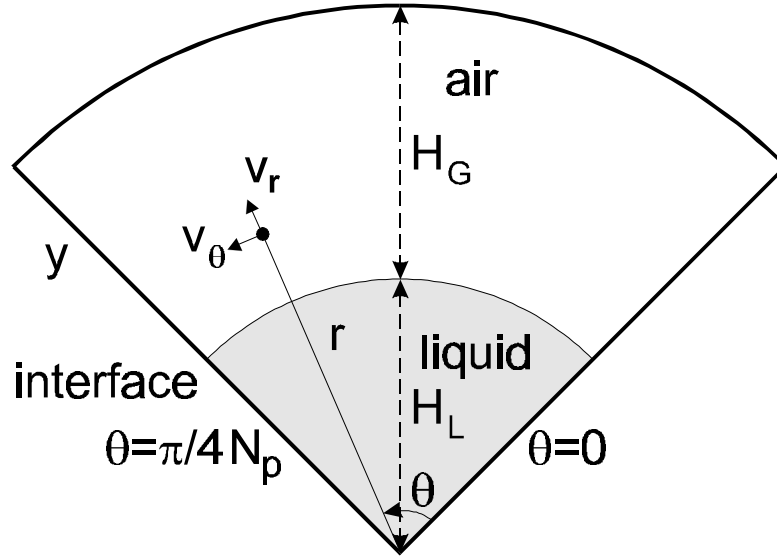


figure 2     *The geometry in case of a convex container. In the experimental case $H_L \approx H_G = 0.0141$ m and $N_p = 2$ (container 4) or $H_L = H_G = 0.02$ m and $N_P = 3$ (container 7).*

For this geometry and these co-ordinates, the dimensionless system of equations takes the following form:

$$v_r = -\frac{1}{r}\frac{\partial \psi}{\partial \theta} \tag{26}$$

$$v_\theta = \frac{\partial \psi}{\partial r} \tag{27}$$

$$\omega = \frac{1}{r}\frac{\partial(v_\theta\, r)}{\partial r} - \frac{1}{r}\frac{\partial v_r}{\partial \theta} \tag{28}$$

$$\frac{\partial \omega}{\partial t} - \frac{1}{r}\frac{\partial \psi}{\partial \theta}\frac{\partial \omega}{\partial r} + \frac{1}{r}\frac{\partial \psi}{\partial r}\frac{\partial \omega}{\partial \theta} = Vi_p\left(\frac{\partial^2 \omega}{\partial r^2} + \frac{1}{r}\frac{\partial \omega}{\partial r} + \frac{1}{r^2}\frac{\partial^2 \omega}{\partial \theta^2}\right) \tag{29}$$

$$\omega = \frac{\partial^2 \psi}{\partial r^2} + \frac{1}{r}\frac{\partial \psi}{\partial r} + \frac{1}{r^2}\frac{\partial^2 \psi}{\partial \theta^2} \tag{30}$$

$$\frac{\partial c}{\partial t} - \frac{1}{r}\frac{\partial \psi}{\partial \theta}\frac{\partial c}{\partial r} + \frac{1}{r}\frac{\partial \psi}{\partial r}\frac{\partial c}{\partial \theta} = \frac{Vi_P}{Sc_P}\left(\frac{\partial^2 c}{\partial r^2} + \frac{1}{r}\frac{\partial c}{\partial r} + \frac{1}{r^2}\frac{\partial^2 c}{\partial \theta^2}\right) \tag{31}$$

Boundary conditions at the solid wall are:

$$\psi = 0 \tag{32}$$

$$\mathbf{n} \cdot \nabla \psi = 0 \tag{33}$$

$$\mathbf{n} \cdot \nabla c = 0 \qquad\qquad \text{(left and right wall)} \tag{34}$$

$$c = 0 \qquad\qquad \text{(permeable top wall)} \tag{35}$$

Boundary conditions at the gas liquid interface:

$$\psi = 0 \tag{36}$$

$$c_{i,G} = c_{i,L} \tag{37}$$

$$\left.\frac{\partial c}{\partial r}\right|_L = Bi_N \left.\frac{\partial c}{\partial r}\right|_G \tag{38}$$

$$\omega_L - \frac{\mu_G}{\mu_L}\omega_G - \frac{2}{r}\left(1 - \frac{\mu_G}{\mu_L}\right)\frac{\partial \psi}{\partial r} = -\frac{Ma}{Sc_L}\frac{1}{r}\frac{\partial c}{\partial \theta} \tag{39}$$

$$\nabla_\Gamma^2 \cdot \psi = 0 \tag{40}$$

$$v_{\theta,L} = v_{\theta,G} \Leftrightarrow \left(\frac{\partial \psi}{\partial r}\right)_L = \left(\frac{\partial \psi}{\partial r}\right)_G \tag{41}$$

## 3.3    Numerical method

The numerical method consists of the following steps. Firstly, a co-ordinate transformation is applied and the governing equations are rewritten for the new co-ordinates. The equations are then centrally discretised, which results in a large set of equations. This large set of equations can not be solved in one step for each time step, since the set is a non-linear one. Therefore, the set is linearised and solved subsequently with Newton iteration. The solution for each Newton iteration is obtained with a conjugate gradient-like method. Before starting the conjugate gradient method, the large set of linearised equations is modified, i.e. the large sparse matrix is preconditioned.

This section starts with the description of the numerical method up to the linearisation for both the flat container and the convex container. Then the linearisation and the Newton iteration are discussed. The numerical method and the model are motivated subsequently. Finally, the accuracy and convergence of the final computer program is addressed.

*Flat container*

From previous numerical experience it was concluded that the use of a triangular geometry would lead to numerical problems in the upper corners of the triangle. Specifically, the mass balance would not be observed in this areas, which would lead to numerical loss of mass. Therefore, it was decided to transform the triangular geometry into a rectangular geometry.

A co-ordinate transformation from x, y to $\eta$, z is made. The transformation is sketched in figure 3.
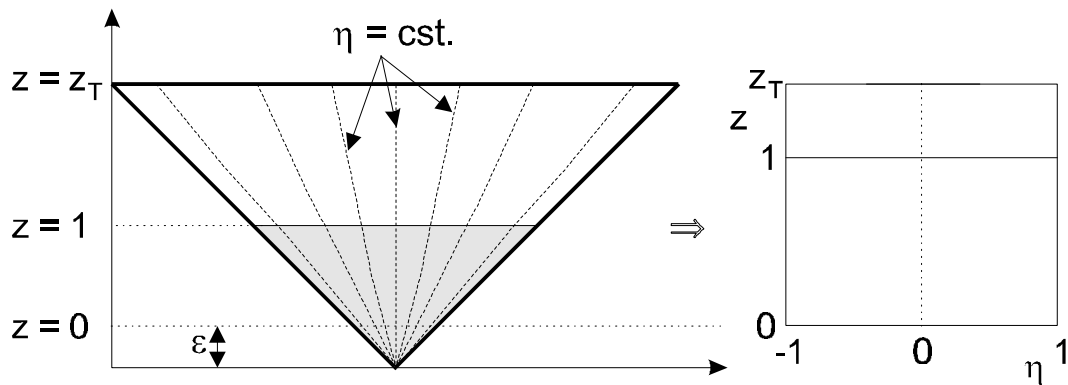


*figure 3    Transformation from the triangular geometry to a rectangular one.*

Furthermore, a transformation from the linear co-ordinate z to the co-ordinate w is made in order to define a non-equidistant grid in the z-direction. The co-ordinate w has been chosen to have the same value as z when z equals 0, 1 and $z_T$. The following equations for w are valid:

$$z = f(w) \qquad\qquad 0 \le z \le 1 \qquad\qquad (42)$$

$$z = g(w) \qquad\qquad 1 \le z \le z_T \qquad\qquad (43)$$

$$f(w) = -a\,w^2 + (1+a)\,w \qquad\qquad (44)$$

$$g(w) = z_T + \frac{b(z_T - w)^2}{(z_T - 1)} - (1 + b)(z_T - w) \qquad\qquad (45)$$

The parameters a and b were usually chosen to be 0.5 or 0.95. The higher the parameter, the more refined the grid is close to the interface. Raising a or b increases the accuracy, but decreases the speed of the calculation. When a or b was chosen too high, unrealistic solutions were obtained.

The governing and boundary equations for the problem were subsequently transformed into the new co-ordinate system, i.e. equations for vorticity, stream function and concentration were written as a function of t, w, and $\eta$. An equidistant grid was defined across the $\eta$,w area,

using the labels $(0..N_\eta, 0..N_{wL})$ for the liquid phase and $(0..N_\eta, N_{wL+1}..N_{wL}+N_{wG})$ for the gas phase (see figure 4). The grid-sizes are:

$$\Delta\eta = \frac{2}{N_\eta} \qquad \Delta w_L = \frac{1}{N_{wL}} \qquad \Delta w_G = \frac{z_T - 1}{N_{wG} - 1} \qquad (46)$$
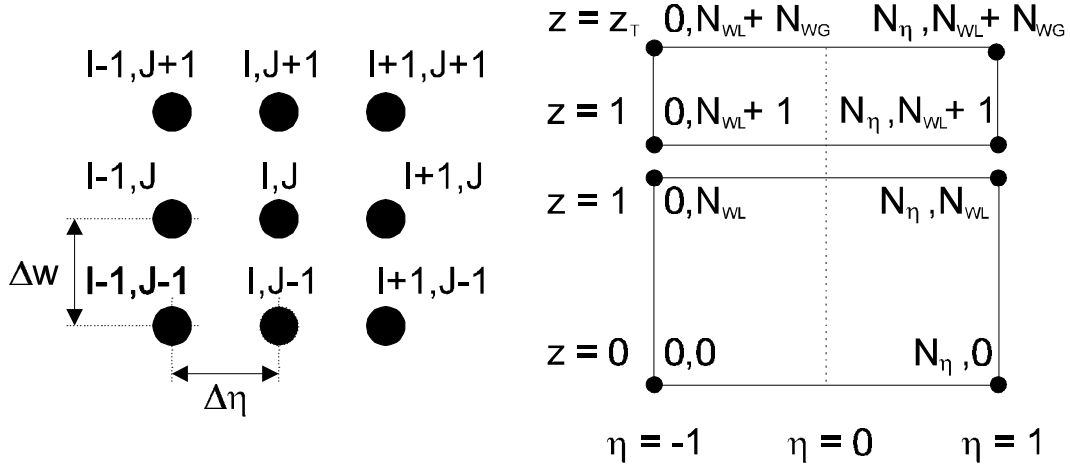


*figure 4    Definition of the equidistant grid used for discretisation.*

The grid points are labelled with i, j and n (referring to $\eta$, w and t respectively) and for the field quantities the following notation is adopted: $\omega_{i,j}^n$, $\psi_{i,j}^n$, and $c_{i,j}^n$.

In discretising the governing equations (5, 17, 18), the product of stream function and concentration or vorticity is discretised as:

$$(\psi c)^{n+1/2} = \frac{1}{4}\left(\psi_{i,j}^n c_{i,j}^n + \psi_{i,j}^{n+1} c_{i,j}^n + \psi_{i,j}^n c_{i,j}^{n+1} + \psi_{i,j}^{n+1} c_{i,j}^{n+1}\right) \qquad (47)$$

The discretised versions of the governing equations are presented in appendix A. The boundary condition for vorticity at the solid wall is analogous to the first-order-accurate formula by Thom [2]. For i = 0, liquid phase, the resulting equation reads:

$$\omega_{i,j}^{n+1} + \psi_{i+1,j}^{n+1}\left\{\frac{4}{\left(\varepsilon + f(w_j)(1-\varepsilon)\right)^2 (\Delta\eta)^2}\right\} = 0 \qquad (48)$$

The discretisation of the boundary condition for concentration at the solid wall and equation (20) is straightforward. Second order forward or backward formulas are used to represent the first derivative of concentration with $\eta$ or w. The boundary condition for liquid phase vorticity at the interface is obtained by centrally discretising the Marangoni boundary condition (21). The boundary condition for the gas phase vorticity is obtained by combining the continuity equation (5) and the no-slip condition (16), resulting in a second-order-accurate formula analogous to that of Wilkes [2]. This formula and its derivation are presented in Appendix B.

When these equations and boundary conditions were used, solutions were obtained with unequal velocities at both sides of the interfaces. Numerically, the following equation should hold for $j = N_{wL}$ :

$$\frac{-1}{f'(1)(1-\varepsilon)}\left(\frac{-4\psi_{i,j-1}^{n+1} + \psi_{i,j-2}^{n+1}}{2\Delta w_L}\right) = \frac{-1}{g'(1)(1-\varepsilon)}\left(\frac{4\psi_{i,j+2}^{n+1} - \psi_{i,j+3}^{n+1}}{2\Delta w_G}\right) \tag{49}$$

This boundary condition was, however, not explicitly present in the set of equations. Therefore, equation (49) was used as an extra boundary condition for $\psi$ for $j = N_{wL+2}$. The continuity equation for this row of grid points had to be dismissed, which introduces only a small error in the mass balance. The approach is justified as the use of the Marangoni boundary condition instead of the continuity equation also introduces a small error in the continuity. In both approaches, approximately the same flow patterns were obtained. In this approach, a small error in the continuity was introduced, while in the other approach the interface is not a strict no-slip boundary.

*Convex container*

The same co-ordinate transformation that was used for y in the case of the flat container was applied for the r co-ordinate in the case of the convex container. The resulting co-ordinate was also labelled w. A similar grid as used for the flat container was applied for the convex container. The gridsizes are now:

$$\Delta\theta = N_P \frac{\pi/2}{N_\theta} \qquad \Delta w_L = \frac{1}{N_{wL}} \qquad \Delta w_G = \frac{z_T - 1}{N_{wG} - 1} \tag{50}$$

The equations were discretised analogous to those for the flat container. The discretised versions of the governing equations are presented in appendix A. The boundary condition for the gas phase vorticity at the interface is presented in appendix B. Again, for first derivatives normal to the boundaries, second-order-accurate forward or backward formulas were used.

*Solving procedure*

For both the flat and the convex container, a system of $N_{eq}$ difference equations exists, for each time step, that needs to be solved:

$$\left.\begin{array}{l} F_1(X_1, X_2, .., X_{N_{eq}}) = 0 \\ F_2(X_1, X_2, .., X_{N_{eq}}) = 0 \\ \quad . \\ \quad . \\ F_{N_{eq}}(X_1, X_2, .., X_{N_{eq}}) = 0 \end{array}\right\} \mathbf{F}(\mathbf{X}) = 0 \tag{51}$$

$$N_{eq} = 3\left(N_\eta \cdot \left(N_{wL} + N_{wG}\right)\right) \qquad \text{or} \quad N_{eq} = 3\left(N_\theta \cdot \left(N_{wL} + N_{wG}\right)\right)$$

To solve this system, the equations were linearised:

$$\mathbf{F}(\mathbf{X}) \approx \mathbf{F}(\mathbf{X_0}) + \mathbf{J}(\mathbf{X} - \mathbf{X_0}) \qquad\qquad (52)$$

$$J_{1,m} = \frac{\partial F_1}{\partial X_m}$$

The solving procedure now consists of the following steps.

- To $\mathbf{X}$ the values at the old time level n are assigned. This is called $\mathbf{X^1}$.
- An iteration parameter k is introduced and the following process is iterated.
- $\mathbf{F}(\mathbf{X^k})$ and $\mathbf{J^k}$ are evaluated. The following expression is solved:

$$\mathbf{J}^k \Delta \mathbf{X}^k = -\mathbf{F}(\mathbf{X}^k) \qquad\qquad (53)$$

- New values are assigned to $\mathbf{X^{k+1}}$:

$$\mathbf{X}^{k+1} = \mathbf{X}^k + \Delta \mathbf{X}^k \qquad\qquad (54)$$

- The iteration is stopped when the following criterion is met:

$$\frac{\sum_{N_{eq}}^{1=0} \left|\Delta X_1^k\right|}{N_{eq} \cdot \overset{max}{_1}\left|X_1^{k+1}\right|} < \varepsilon_1 \qquad\qquad (55)$$

For $\varepsilon_1$ a value of $1\ 10^{-10}$ was chosen.

Equation (53) was solved with a conjugate gradient iterative method, called GMRES. This method is described in detail by Van der Ploeg [3]. This iteration was stopped when the two norm of the residual was smaller than $\varepsilon_2$. The value of $\varepsilon_2$ was chosen to be $1\ 10^{-3}$. Convergence for the Newton iteration was observed to be faster when a less accurate solution of the conjugate gradient method was accepted, up to a certain bound. The convergence of the GMRES solver was accelerated by preconditioning the matrix $\mathbf{J}$. The matrix $\mathbf{J}$ was splitted in the factors $\mathbf{L}$ and $\mathbf{U}$ and the residual matrix $\mathbf{R}$; $\mathbf{J} = \mathbf{LU} + \mathbf{R}$. The factors $\mathbf{L}$ and $\mathbf{U}$ are sparse and all the elements of the matrix $\mathbf{R}$ are in absolute value smaller than a pre-set threshold parameter, which varies in this case between $10^{-6}$ and $10^{-8}$. The smaller this threshold parameter, the longer the construction of the factors $\mathbf{L}$ and $\mathbf{U}$ and the larger the memory requirements, but the better the convergence of the GMRES procedure. New factors $\mathbf{L}$ and $\mathbf{U}$ were constructed when k > 30 for one time step, or when the number of iterations for each conjugate gradient iteration exceeded 70. Details of this preconditioning technique are described by Van der Ploeg [3]. It should be noted that the use of this preconditioning technique was essential to the solution of equation (53) in terms of speed and convergence.

*Initial conditions*

For both cases the following initial conditions apply:

$$\psi_{i,j}^0 = 0 \qquad\qquad \forall\, i, j \qquad\qquad (56)$$

$$\omega_{i,j}^0 = 0 \qquad\qquad \forall\, i, j \qquad\qquad (57)$$

$$c_{i,j}^0 = 1 \qquad\qquad \forall\, i, j \leq N_{wL+1} \qquad\qquad (58)$$

$$c_{i,j}^0 = 0 \qquad\qquad \forall\, i, j > N_{wL+1} \qquad\qquad (59)$$

For the convex container, flow is expected as a result of amplification of disturbances. Numerically, these disturbances were introduced by introducing the following initial concentration distribution for the interface:

$$c_{i,j}^0 = 1 - X_{dist} \left| \frac{\mod\left( i, \frac{2N_\theta}{N_{dist}} \right) \cdot N_{dist}}{N_\theta} - 1 \right| \qquad \forall\, i, j = N_{wL}, N_{wL+1} \qquad (60)$$

In this equation, the function mod is defined as the Fortran function MOD, and $X_{dist}$ and $N_{dist}$ were usually chosen 0.0001 and 6, respectively. This approach was preferred over other ways for introducing a numerical disturbance for practical reasons. Other approaches are the introduction of a randomly disturbed interface concentration or the introduction of a disturbance with a wavelength that corresponds to the most unstable wavelength found when a linear stability analysis is carried out [4]. The latter method involves additional work, and does not guarantee the use of the "right wavelength" encountered in physical reality. A randomly disturbed interface concentration prevents the direct comparison between various calculations. Various values for $X_{dist}$ and $N_{dist}$ were used, and it was found that the same macroscopic convective patterns evolved after some initial time (see section 3.5).

The large initial concentration gradients imposed by these boundary conditions introduce numerical problems at the interface for short times. Therefore, slightly different initial conditions were used. Using equations (56-60) for a specific set of parameters Ma, $Sc_L$, $Sc_G$, $Bi_N$, $Vi_G$, $\mu_G$, $\mu_L$, a calculation was performed for 500 time steps, setting Ma = 0, each time step being $1\ 10^{-5}$. The resulting concentration distribution was used as the initial concentration distribution for the remainder of the calculation (with Ma $\neq$ 0). In this way, the concentration distribution was somewhat smoothed, and numerical problems due to large initial gradients were avoided.

*Motivation of the model and the numerical method*

The model used by Hoogstraten et al. [1] was similar to the model described above. However, as in many other models describing the development of Marangoni flows in gas-

liquid systems [e.g. 5, 6], the gas phase was only taken into account by introducing the following boundary condition at the interface:

$$\frac{\partial c}{\partial y} = Bi_R \, c \qquad\qquad (61)$$

$$Bi_R = \frac{m D_G H_L}{H_G D_L} \quad \text{or: } Bi_R = \frac{k H_L}{D_L} \quad \text{or: } Bi_R = \frac{m H_L}{R_G D_L} \qquad\qquad (62)$$

In these equations, k is a mass transfer coefficient and $R_G$ is the mass transfer resistance of the gas phase. This approach has the following shortcomings:

1.  The Biot number $Bi_R$ is a place and time-dependent parameter. This is taken care of automatically when the gas phase is taken into account. In the single phase approach, however, an estimation for this Biot number as a function of time and place has to be made (see [5, 7]). Often, nevertheless, this Biot number is assumed to be fixed [1]. The shortcoming of the use of the empirical Biot number in thermocapillary convection problems was already recognised by Simanovskii and Nepomnyashchy [8].

2.  Diffusion parallel to the interface through the gas phase is ignored. This could lead to significant errors, as the diffusion coefficient in the gas phase is usually four orders of magnitude larger than the diffusion coefficient in the liquid phase. The larger diffusion coefficient in the gas phase leads to faster concentration equilibration parallel to the interface, and disturbances in the concentration field parallel to the interface penetrate much further, which leads to different roll cell sizes.

3.  Convection in the gas phase also contributes to pattern selection and mass transfer. Since the diffusivity is in the order of $10^{-5}$ m$^2$/s, convection is only relevant in the 1 cm geometry when velocities start to exceed 1 mm/s. This is the case for the microgravity experiments, but it does not apply for most studies. Usually, only slightly supercritical Marangoni numbers are used, which implies relatively low velocities.

    Furthermore, according to the Sternling-Scriven criteria, the system used in these calculations falls into the stationary unstable, diffusion controlled, regime [9]. Neglecting the convection in the gas phase has less influence than neglecting the diffusive contribution of the gas phase. However, for some cases convection in the gas phase can not be ignored. An example of such a case concerns the situation in which acetone absorbs in the water phase instead of desorbing from it (reversed mass transfer, see chapter 2). In that case, the system is in the oscillatory unstable, convection controlled regime.

Some calculations have been performed on a one phase system as described by Hoogstraten et al. [1], using the numerical method presented in this chapter. For the flat container, very small roll cells were initially found in the corners. Since the concentration distribution in the middle of the container is not disturbed by the concentration sink in the corners due to the low liquid phase diffusivity, these roll cells did not extend over the entire container. The small roll cells initiated large, counter rotating roll cells in the middle of the

container, which turn the opposite way as was found experimentally. Furthermore, the combination of high velocities and low diffusivities at the interface was found to introduce numerical problems (wiggles etc.) at the interface for lower Marangoni numbers than those that caused numerical problems in the two phase model. The one phase model was therefore dismissed.

Regarding the choice of the numerical method, a few words need to be said. As described in the introduction of section 3.2, an A.D.I. method was first employed that was not completely implicit. Very small time steps were required as the numerical system was unstable, and only relatively small Marangoni numbers were possible. Especially, the Thom boundary condition for vorticity (equation 48) was very sensitive to this instability. The present method circumvents this problem as the whole system of equations is solved simultaneously. Boundary conditions and governing equations linking the field quantities concentration, vorticity and stream function can be incorporated without resorting to the use of values of these quantities at the previous time level. The use of the preconditioning technique, developed by the Mathematical Institute of the University of Groningen, proves to be invaluable to the solution of the matrix equation (53). This method is therefore expected to be valuable in other problems, in which the field quantities are linked in the system equations, as in, for example, (double-diffusive) Rayleigh-Marangoni problems and Soret problems. Other numerical techniques, as for example the one referred to in a paper on solutal Marangoni convection in a system with two melt phases by Yasuhiro et al. [10], might however also yield satisfactory results.

*Accuracy and convergence*

Convergence of the computer program was checked for a few model situations and the method was found to be first-order in time and second-order in both spatial co-ordinates. The accuracy was checked by solving a few problems with different time steps, grid sizes and values of a and b. Solutions for interface quantities, such as interface velocities and concentrations, proved to be almost exactly the same for the case a = 0.508 ; $N_{wL} = 60$ and the case a = 0 ; $N_{wL}$ =120. From equation (44) this is also expected, as the grid size near the interface is the same in both cases.

In figure 5, solutions for $Sc_L = 791$; $Sc_G = 1.48$; $Ma = 10^5$; $Bi_N = 13.1$; $Vi_G = 15.38$; $\mu_G/\mu_L = 1.826 \ 10^{-2}$; $N_{wL} = 60$; $N_{wG} = 31$; $N_\eta = 60$; $H_L = H_G$; a = b = 0.5 are compared for $\Delta t = 5 \ 10^{-3}$ and number of time steps $N_t = 400$ (figure 5a,b) and $\Delta t = 5 \ 10^{-4}$ and $N_t = 4000$ (figure 5c,d). Almost the same solutions are obtained.
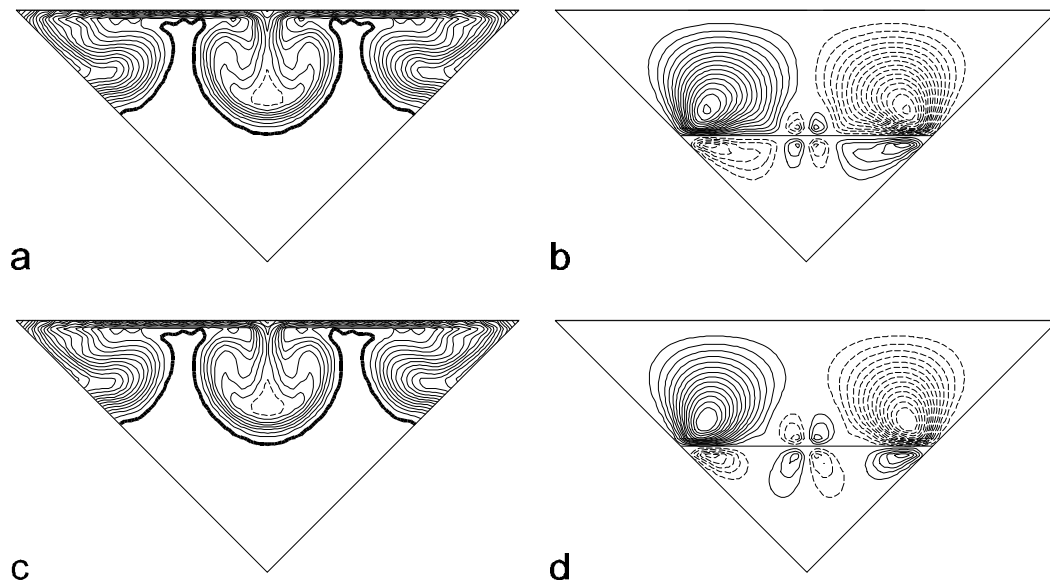
*figure 5*    *Comparison for different time steps. See text for parameter values. a. Isoconcentration plot for $Dt = 5\ 10^{-3}$ ; $N_t = 400$; $D_C = 0.02$; $C_{max} = 0.99$; b. Contourplot for same case; $D_S = 0.01$; c. Isoconcentration plot for $Dt = 5\ 10^{-4}$ ; $N_t = 4000$; $D_C = 0.02$; $C_{max} = 0.99$; d. Contourplot for same case; $D_S = 0.01$. See text on next page for explanation regarding the presentation of these results.*
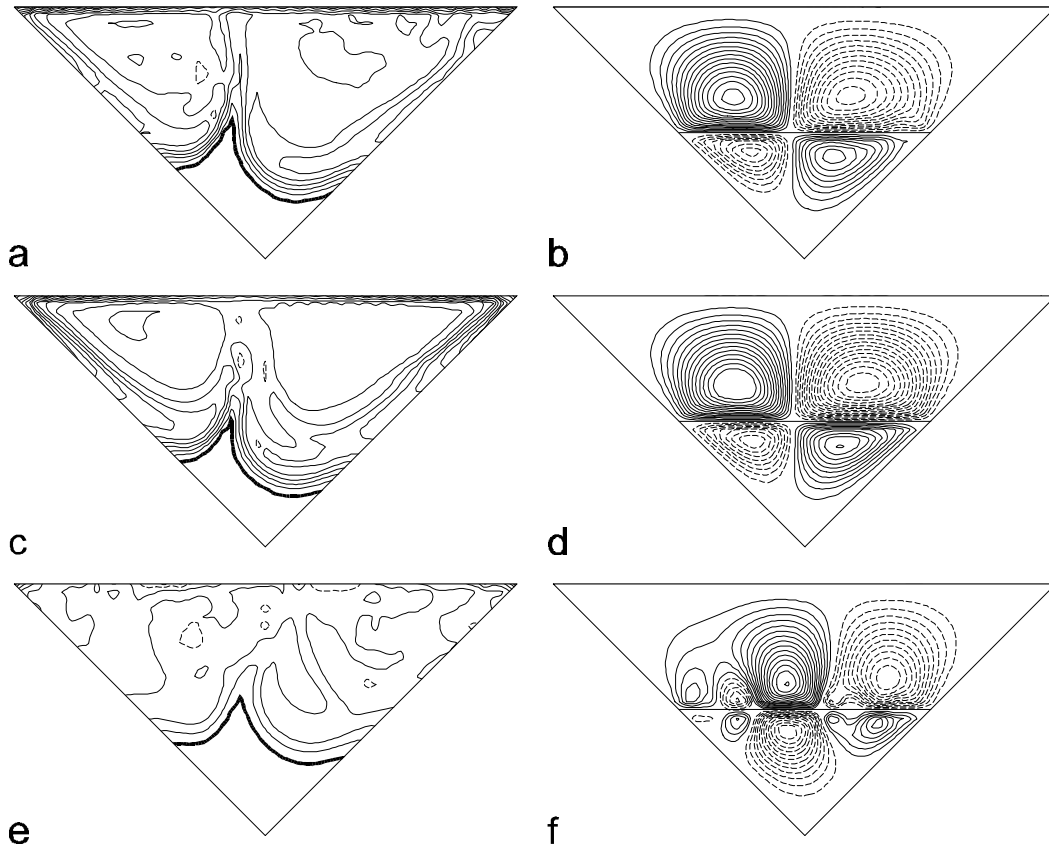
*figure 6*        *Comparison for different grids. See text for parameter values. a. Isoconcentration plot for $N_h$ = 60; $N_{wL}$ = 60; $N_{wG}$ = 31; $Dt$ = 5 $10^{-3}$; $N_t$ = 400; a = b = 0.5; $D_C$ = 0.02; $C_{max}$ = 0.99; b. Contourplot for same case; $D_S$ = 0.1; c. Isoconcentration plot for $N_h$ = 150; $N_{wL}$ = 90; $N_{wG}$ = 31, $Dt$ = 5 $10^{-4}$; $N_t$ = 4000; a = b = 0.5; $D_C$ = 0.02; $C_{max}$ = 0.99; d. Contourplot for same case; $D_S$ = 0.1; e. Isoconcentration plot for $N_h$ = 60; $N_{wL}$ = 60; $N_{wG}$ = 31, $Dt$ = 1 $10^{-3}$; $N_t$ = 2000; a = b = 0.95; $D_C$ = 0.02; $C_{max}$ = 0.99; f. Contourplot for same case; $D_S$ = 0.1*

For the presentation of the results (contour plots), the following convention is adopted. In the stream function plots, dotted lines indicate negative stream function values, and continuous lines indicate positive stream function values. Negative values indicate an anti-clockwise turning roll cell, positive values a clockwise turning roll cell. In the caption to the figure, the increase in value between each streamline is indicated by the quantity $\Delta_S$ (dimensionless). Contour lines for zero stream function are omitted. In the concentration plots, the maximum contour line is indicated with a thick black line. Dotted lines point to a (local) minimum value of concentration. The increase in value between each iso-concentration line is indicated in the caption by the quantity $\Delta_C$ (dimensionless). The value corresponding to the maximal concentration contour line is indicated by the quantity $C_{max}$ (dimensionless). Note that for the stream function plots, both the liquid and the gas phase are presented, while for the concentration plots, only the liquid phase is presented.

In figure 6, results are presented for the physical parameters described above, but Ma = $10^6$. In one case, $N_\eta = 60$, $N_{wL} = 60$, $N_{wG} = 31$, $\Delta t = 5 \ 10^{-3}$, $N_t = 400$, a = b = 0.5 (figure 6a, b), for another case $N_\eta = 150$, $N_{wL} = 90$, $N_{wG} = 31$, $\Delta t = 5 \ 10^{-4}$, $N_t = 4000$, a = b = 0.5 (figure 6c, d), and for a third case $N_\eta = 60$, $N_{wL} = 60$, $N_{wG} = 31$, $\Delta t = 1 \ 10^{-3}$, $N_t = 2000$, a = b = 0.95 (figure 6e, f). In figure 7, the evolution of the maximum interface velocity with time is depicted for these three cases. From these results it can be seen that the results are dependent on the grid, especially on the refinement of the grid, but that qualitatively the same results are obtained. For higher values of a and b, the situation near the interface is described more accurately, which leads to steeper concentration gradients and higher velocities. The total mass of acetone in the container, obtained by integrating the concentration over the total liquid volume, decreases less fast for more accurate grids, again as a result of the more accurate representation of physical reality near the interface. Similar results were obtained for the convex container. Convergence takes longer for higher a and b, and therefore not all the calculations have been done with these higher values of a and b.
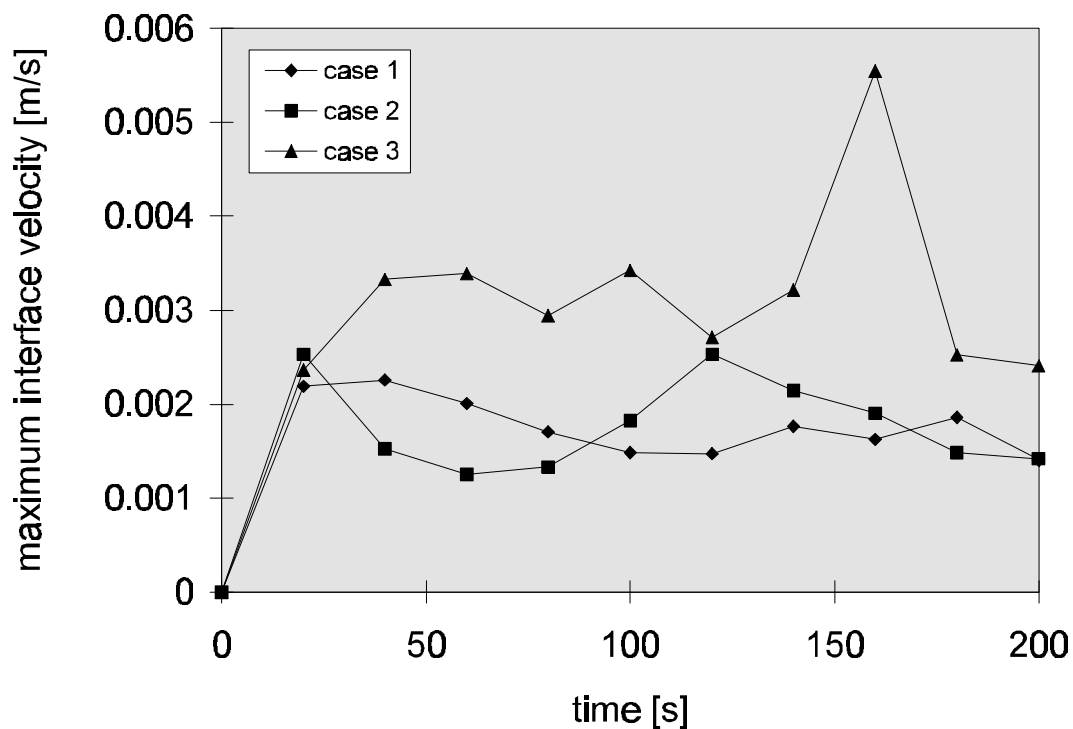


*figure 7        Comparison for different grids. Maximum interface velocity as a function of time for $H_L = H_G = 0.01$ cm. Same cases as described for figure 6.*

### 3.4     Results for flat container

In the remainder of this chapter, the following physical properties and the resulting dimensionless numbers are used: $D_L = 1.27 \ 10^{-9}$ m²/s [11], $D_G = 1.04 \ 10^{-5}$ m²/s [11], $\mu_L = 1.002 \ 10^{-3}$ Pa s [12], $\mu_G = 1.83 \ 10^{-5}$ Pa s [12], $\nu_L = 1.004 \ 10^{-6}$ m²/s [12], $\nu_G = 1.5443 \ 10^{-5}$ m²/s [12], $H_L = 0.0141$ m, $H_G = 0.0141$ m, $m = 1.60 \ 10^{-3}$ [kg/m³ m³/kg] [13], $Bi_N = 13.1$, $Sc_L = 791$, $Sc_G = 1.48$ and $Vi_G = 15.38$. The Marangoni number is varied. It should be kept in mind that the real Marangoni number for the experimental system, given $(d\gamma/dc) = -1.6 \ 10^{-4}$ m³/s² [14] and $c_0 \approx 50$ kg/m³ (see chapter 2), is approximately $8.9 \ 10^7$. Note that the dependence of surface tension on concentration depends strongly on the absolute concentration, whereby this dependence is larger for lower concentrations. The parameter $\varepsilon$ (figure 3) is set to 0.05.

Calculations were performed on the Cray-J90 of the Faculty of Mathematics and Science of the University of Groningen and on three different HP machines of the Department of Chemistry of the University of Groningen.

*Different Marangoni numbers*

For the parameters described above, various runs were carried out in which the Marangoni number was steadily increased. Calculations were performed up to Ma = $2 \ 10^7$. Runs were performed for various values of a, b, Ma, $\Delta t$ and $N_t$. The runs described here were all performed on a grid with $N_\eta = 60$, $N_{wL} = 60$, $N_{wG} = 31$. The runs presented in this chapter are summarised in table 1.

*Table 1.     Parameter values for runs with flat container.*

|        | Ma | a | b | $\Delta t$ | $N_t$ |
|--------|------|------|------|----------|-------|
| Case 1 | $1 \ 10^3$ | 0.95 | 0.95 | $5 \ 10^{-3}$ | 400 |
| Case 2 | $1 \ 10^4$ | 0.95 | 0.95 | $5 \ 10^{-3}$ | 400 |
| Case 3 | $1 \ 10^5$ | 0.95 | 0.95 | $5 \ 10^{-3}$ | 400 |
| Case 4 | $1 \ 10^6$ | 0.95 | 0.95 | $1 \ 10^{-3}$ | 2000 |
| Case 5 | $1 \ 10^5$ | 0.5 | 0.5 | $2 \ 10^{-4}$ | 5000 |
| Case 6 | $1 \ 10^6$ | 0.5 | 0.5 | $2 \ 10^{-5}$ | 50000 |
| Case 7 | $5 \ 10^6$ | 0.5 | 0.5 | $2 \ 10^{-5}$ | 50000 |
| Case 8 | $1 \ 10^7$ | 0.5 | 0.5 | $2 \ 10^{-5}$ | 50000 |
| Case 9 | $2 \ 10^7$ | 0.5 | 0.5 | $2 \ 10^{-5}$ | 45000 |

Runs for higher values of the Marangoni number have been tried, but extremely small time steps were necessary to achieve convergence. A larger grid could have been a solution to

this problem, but the combination of small time steps and large grids would require extremely long calculation times. From the runs that have been tried, it was found that interface velocities in the order of several cm/s or even dm/s were found (after a few seconds real time) for Ma numbers approaching $10^8$. This clearly did not correspond to the experimentally found maximum interface velocity of roughly 0.6 cm/s for a flat container in microgravity (container 5, see chapter 2).

It should be kept in mind that all dimensional values, which are presented along with the results, are valid for $H_L = H_G = 0.0141$ m, but that the results apply also for any other value of $H_L$ (with equal $H_G$). The times mentioned in the captions to the figures should then be multiplied with ($H_L^2 / 0.0141^2$) and velocities multiplied by ($0.0141 / H_L$).

Results for a = b = 0.95 are presented in figures 8-11. Results for a = b = 0.5 are presented in figures 12-16. In figure 17, maximum interface velocities are presented as a function of time for all the different cases. The calculation time for case 9 was approximately 2 $10^6$ CPU seconds on the Cray-J90. Results are discussed in section 3.6.
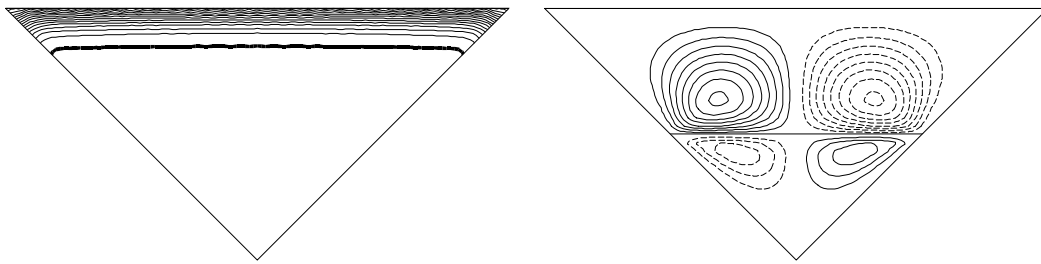


*figure 8*     *Evolution of concentration field (left) and flowpattern (right) for the flat container, $H_L = H_G = 0.0141$ m. Case 1 (Ma = $10^3$) after 400 seconds. $C_{max} = 0.99$; $D_C = 0.04$; $D_S = 0.0002$*
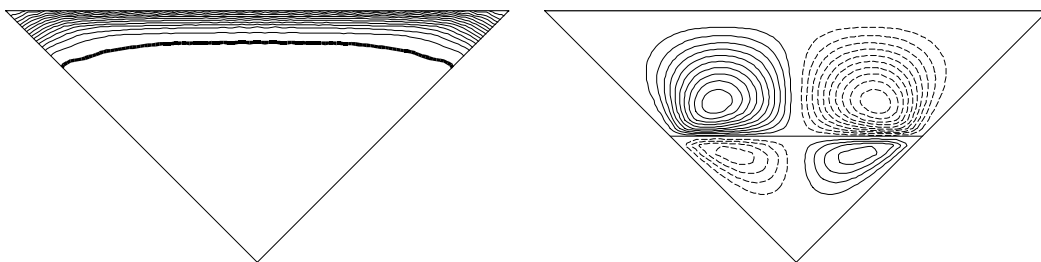


*figure 9*     *Evolution of concentration field (left) and flowpattern (right) for the flat container, $H_L = H_G = 0.0141$ m. Case 2 (Ma = $10^4$) after 400 seconds. $C_{max} = 0.99$; $D_C = 0.04$; $D_S = 0.002$*
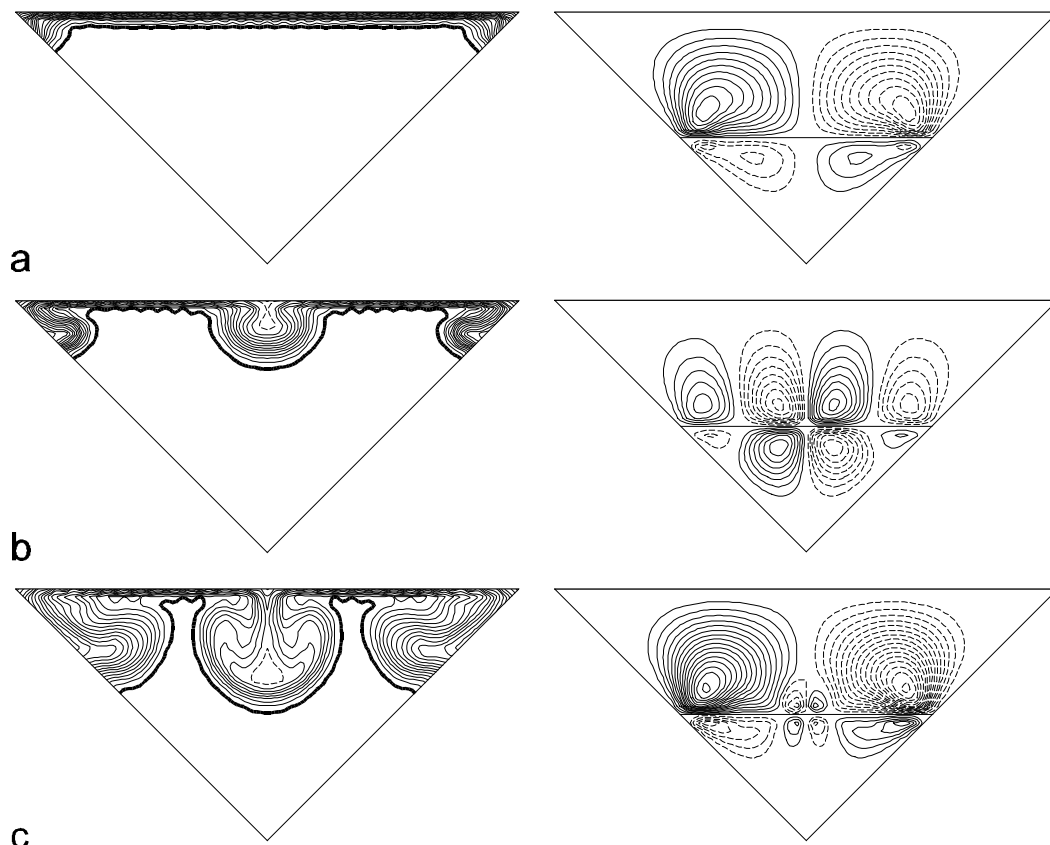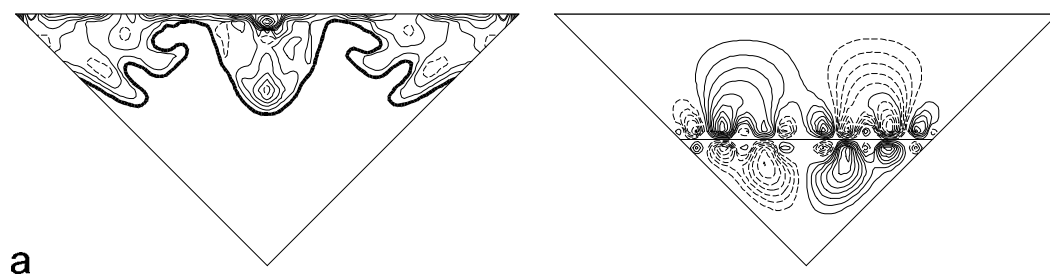
figure 10    *Evolution of concentration field (left) and flowpattern (right) for the flat container,* $H_L = H_G = 0.0141$ *m, case 3 (Ma = $10^5$). For all iso-concentration plots $C_{max} = 0.99$; $\mathbf{D}_C = 0.02$. a. After 80 seconds; $\mathbf{D}_S = 0.01$; b. After 160 seconds; $\mathbf{D}_S = 0.02$; c. After 400 seconds; $\mathbf{D}_S = 0.01$*



figure 11    *Evolution of concentration field (left) and flowpattern (right) for the flat container,* $H_L = H_G = 0.0141$ *m, case 4 (Ma = $10^6$). For all iso-concentration plots $C_{max} = 0.99$. a. After 80 seconds $\mathbf{D}_C = 0.01$; $\mathbf{D}_S = 0.04$.*
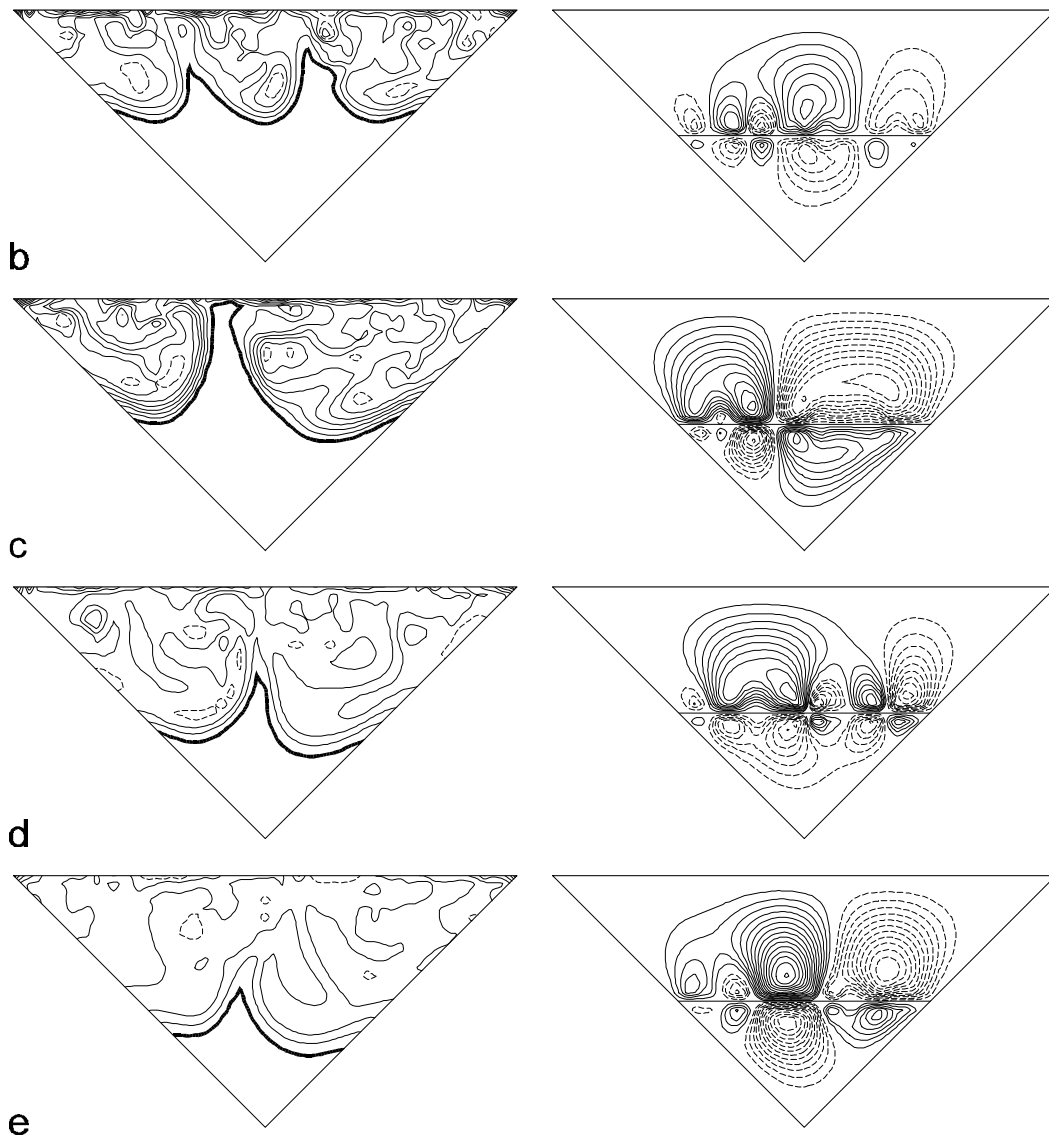
b

c

d

e

*figure 11*    *b. After 160 seconds $D_C$ = 0.01; $D_S$ = 0.1; c. After 240 seconds $D_C$ = 0.01;*
             *$D_S$ = 0.1; d. After 320 seconds $D_C$ = 0.02; $D_S$ = 0.1; e. After 400 seconds*
             *$D_C$ = 0.02; $D_S$ = 0.1.*
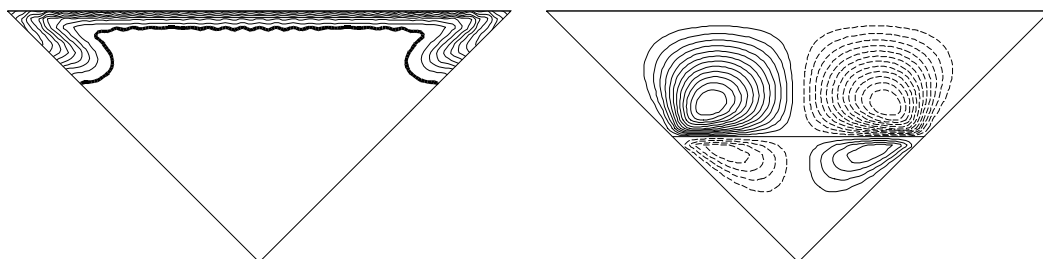


*figure 12*    *Evolution of concentration field (left) and flowpattern (right) for the flat*
             *container, $H_L$ = $H_G$ = 0.0141 m. Case 5 (Ma = $10^5$) after 200 seconds.*
             *$C_{max}$ = 0.99; $D_C$ = 0.04; $D_S$ = 0.01*

*figure 13*    *Evolution of concentration field (left) and flowpattern (right) for the flat container, $H_L = H_G = 0.0141$ m, case 6 (Ma = $10^6$). For all plots $C_{max} = 0.99$; $\boldsymbol{D}_C = 0.02$; $\boldsymbol{D}_S = 0.1$. a. After 80 seconds; b. After 160 seconds*
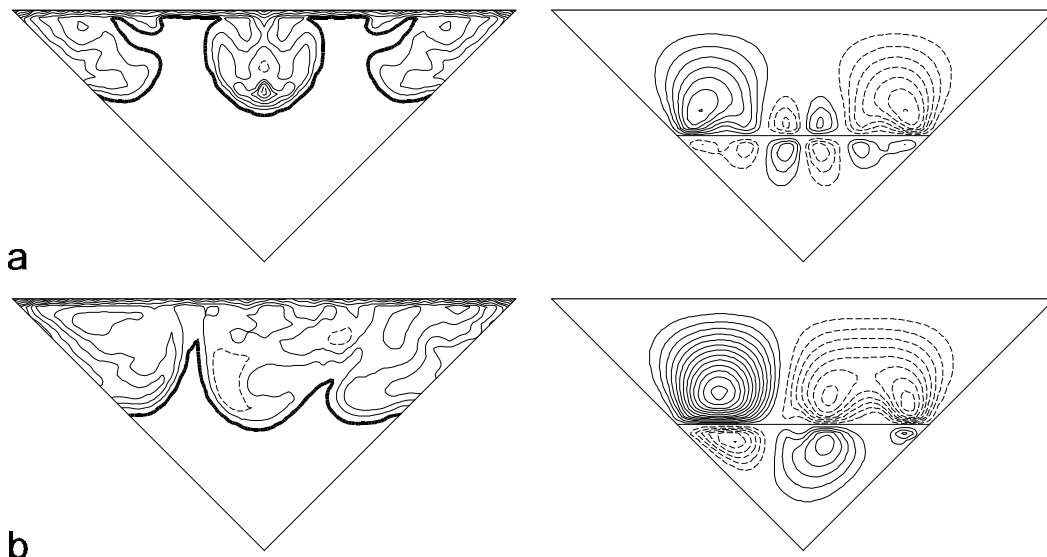


*figure 14*    *Evolution of concentration field (left) and flowpattern (right) for the flat container, $H_L = H_G = 0.0141$ m, case 7 (Ma = 5 $10^6$). For all plots $C_{max} = 0.99$; $\boldsymbol{D}_C = 0.01$; $\boldsymbol{D}_S = 0.4$. a. After 80 seconds; b. After 160 seconds*

*figure 15    Evolution of concentration field (left) and flowpattern (right) for the flat container, $H_L = H_G = 0.0141$ m, case 8 (Ma = $10^7$). For all plots $C_{max} =$ 0.99; $D_C = 0.01$; $D_S = 0.4$. a. After 80 seconds; b. After 160 seconds.*
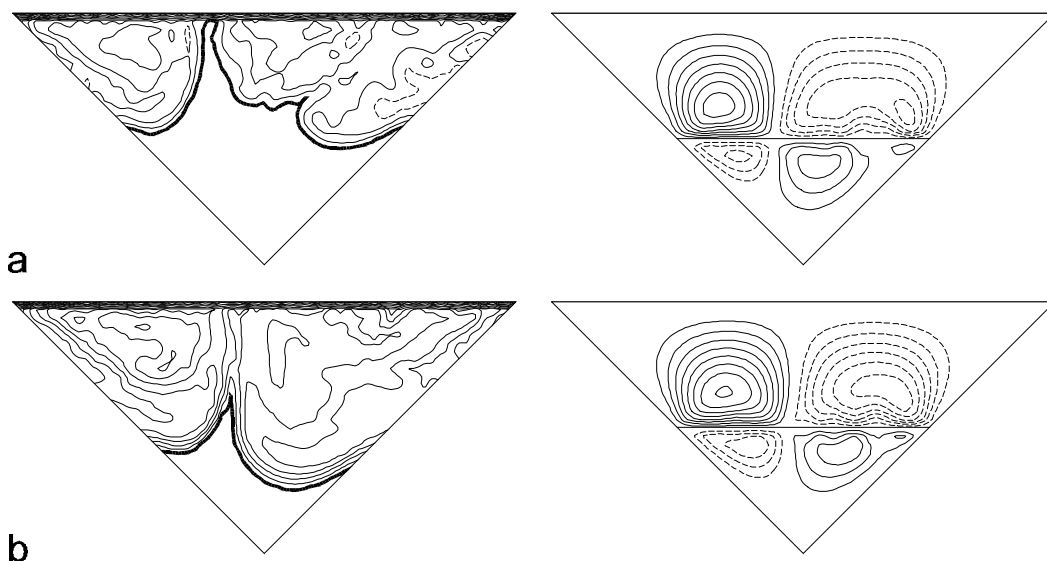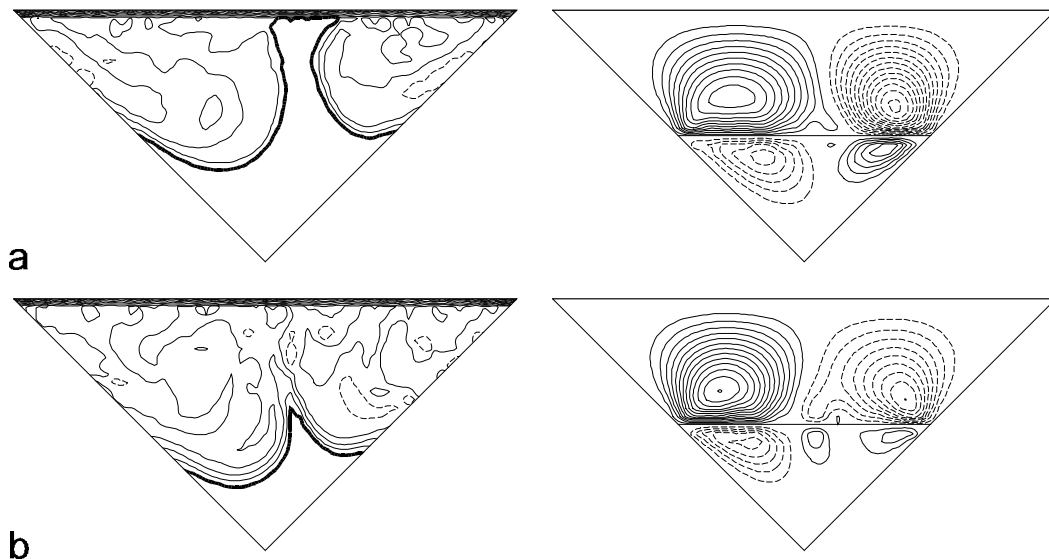


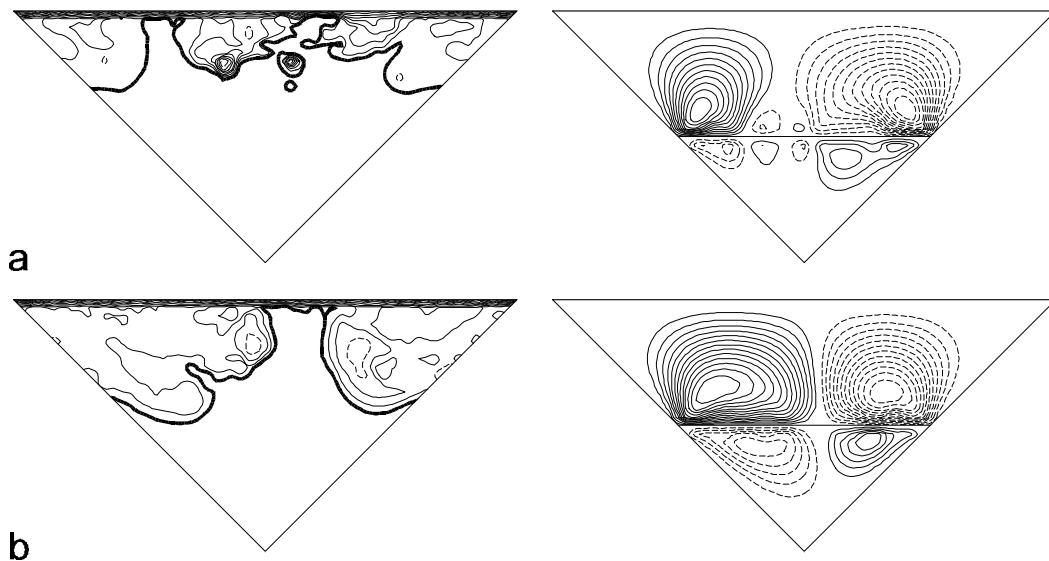*figure 16    Evolution of concentration field (left) and flowpattern (right) for the flat container, $H_L = H_G = 0.0141$ m, case 9 (Ma = 2 $10^7$). For all plots $C_{max} =$ 0.99; $D_C = 0.01$; $D_S = 0.4$. a. After 20 seconds; b. After 40 seconds.*
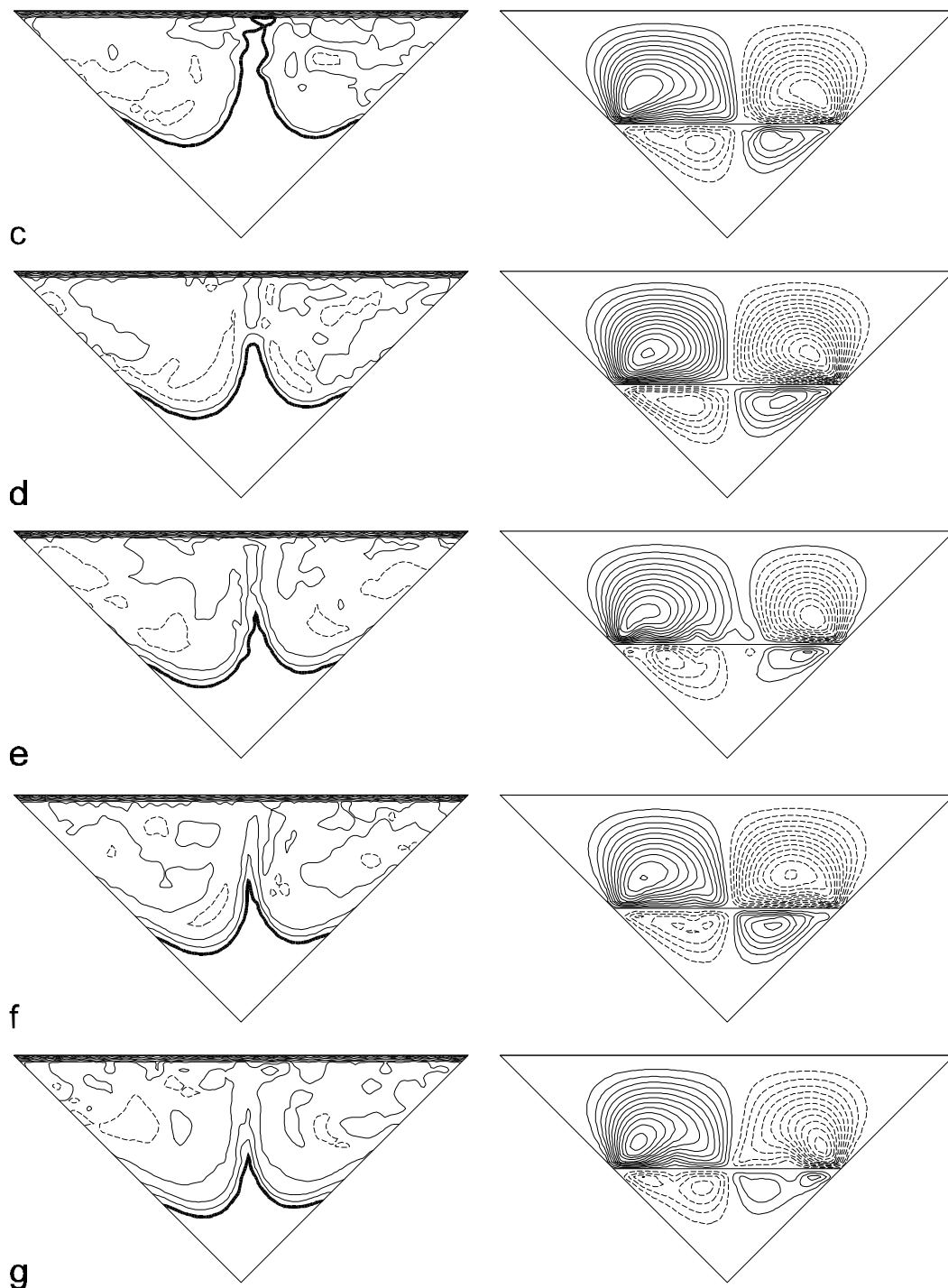
*figure 16     c. After 60 seconds; d. After 80 seconds; e. After 100 seconds; f. After 120 seconds; g. After 140 seconds.*
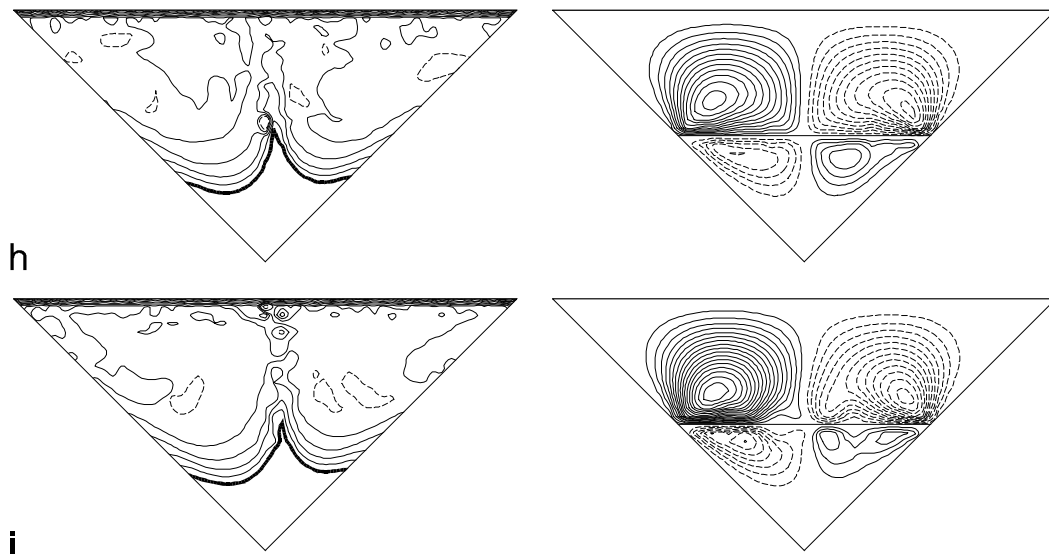
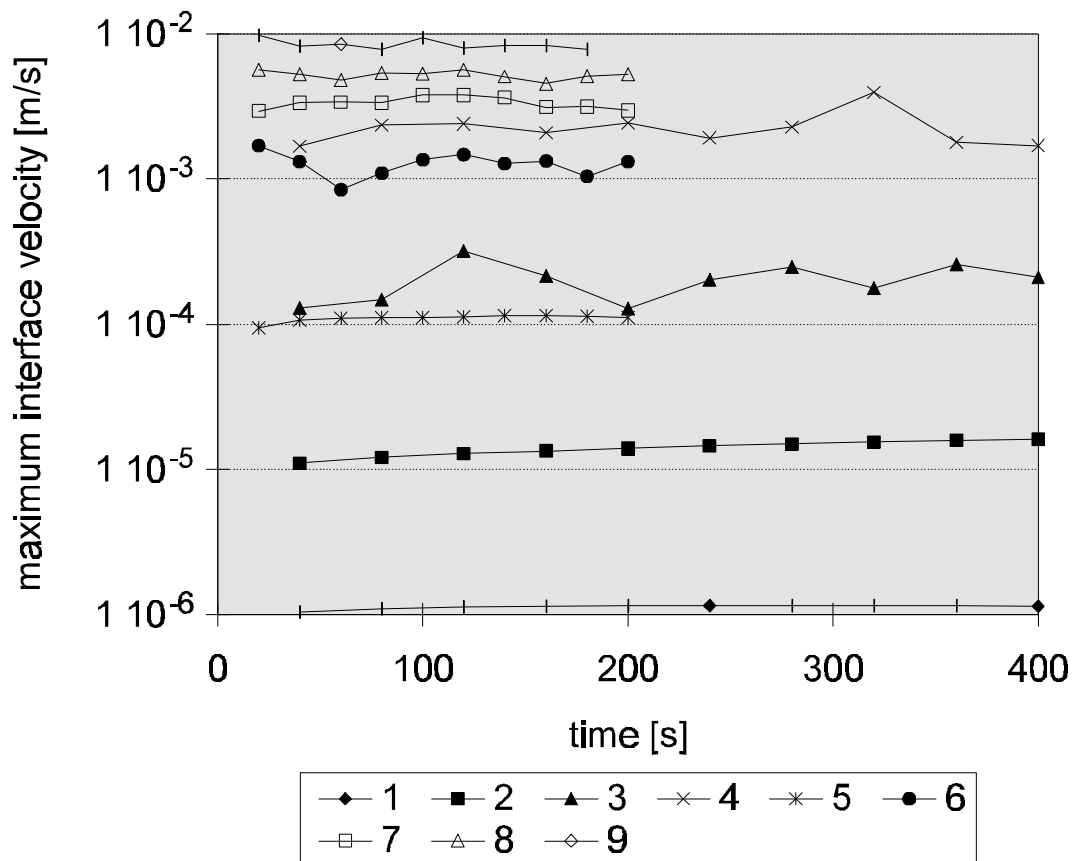*figure 16    h. After 160 seconds; i. After 180 seconds*



*figure 17    Maximum interface velocities as a function of time for the different cases (flat container). Each legend number corresponds to its respective case.*

## 3.5    Results for convex container

In this section, predominantly the results are presented for a container making up one quarter of a cylinder with the parameters $H_L = H_G = 0.0141$ m and $N_p = 2$. This container is quite similar to the container 4 described in chapter 2 (see page 38).

*Different numerical disturbances*

To investigate the influence of the nature of the numerical disturbances on the evolution of the Marangoni flow in the convex containers, six different runs have been performed with different values for the parameters $X_{dist}$ and $N_{dist}$ introduced in equation (60). The parameter values are listed in table 2.

Table 2.     *Parameter values for runs with different initial conditions for the convex container (a = b = 0.5; **D**t = 5 10⁻⁴; $N_q = 60$, $N_t = 4000$):*

|  | Ma | $N_{dist}$ | $X_{dist}$ |
|---|---|---|---|
| Case ri1 | $10^7$ | 6 | 0.0001 |
| Case ri2 | $10^7$ | 5 | 0.0001 |
| Case ri3 | $10^7$ | 6 | 0.001 |
| Case ri4 | $10^7$ | 6 | 0.01 |
| Case ri5 | $10^7$ | 12 | 0.0001 |
| Case ri6 | $10^7$ | 6 | -0.0001 |

From the results, it can be concluded that in each of the cases described above, a final (after 400 seconds) two roll cell pattern evolves in which the liquid flows along the interface from the middle of the container to the sides. In case ri2 and ri6, the initial boundary conditions impose roll cells which turn exactly the other way around. However, after 40 seconds, in all the cases, only roll cell patterns with roll cells of the former type survive (see also chapter 2). The patterns consist of four to eight roll cells in the liquid. After 80 seconds, all but one of the patterns (case ri4: 4 roll cells) develop into a two roll cell pattern. These observations lead to the contention that the initial conditions do have an influence on the shape of the intermediate convective patterns, but that all different initial conditions eventually lead to the same kind of two roll cell pattern. Calculated velocities are of the same order of magnitude, which is demonstrated in figure 18. In figure 19, the concentration distributions after 400 seconds are shown for all the different cases.
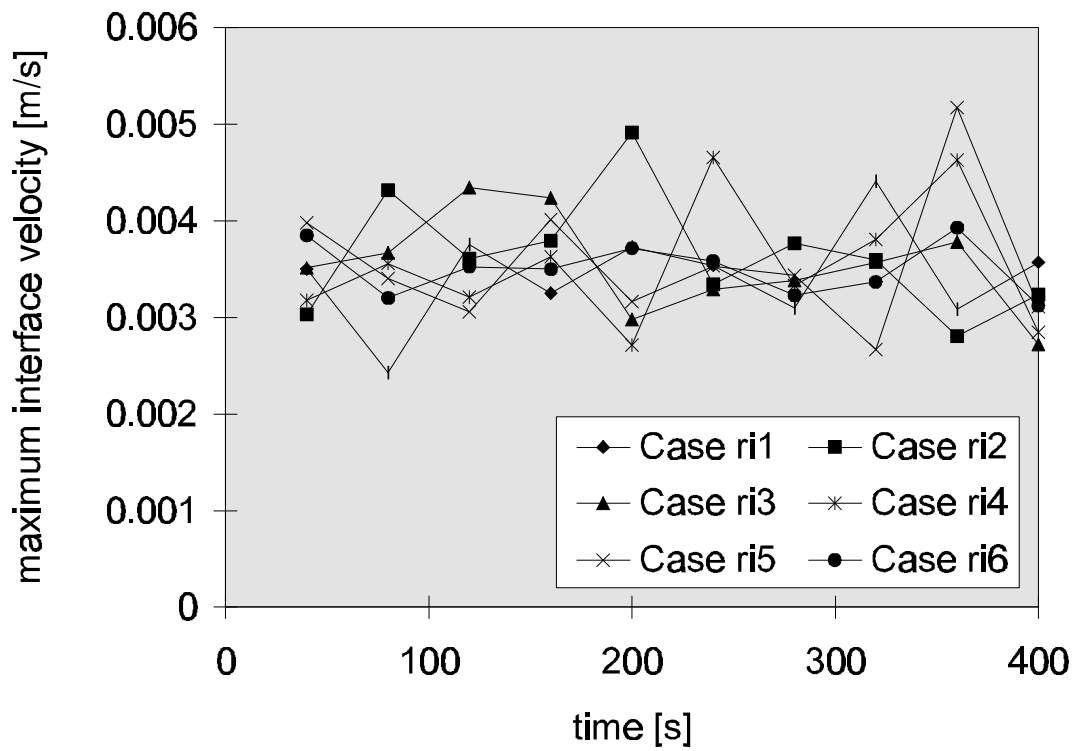
*figure 18   Maximum velocities at the interface as a function of time for different initial conditions.*
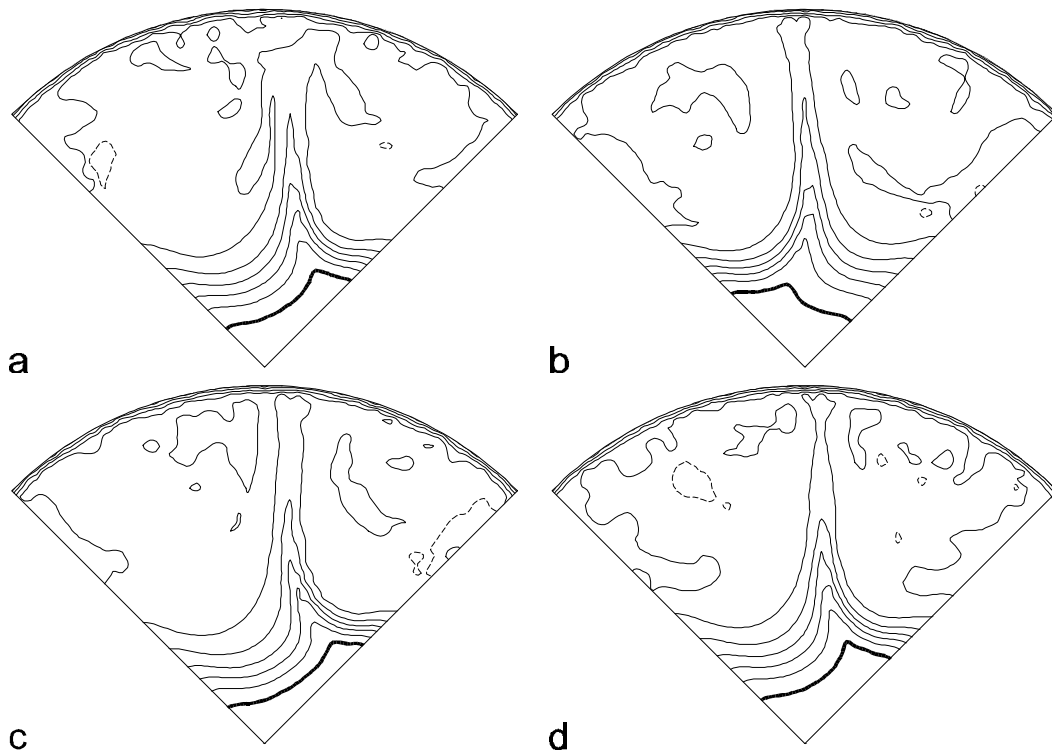


*figure 19   Concentration field for different initial conditions after 400 seconds. For all plots $C_{max} = 0.99$; $\mathbf{D}_C = 0.02$. a. Case ri1; b. Case ri2; c. Case ri3; d. Case ri4*
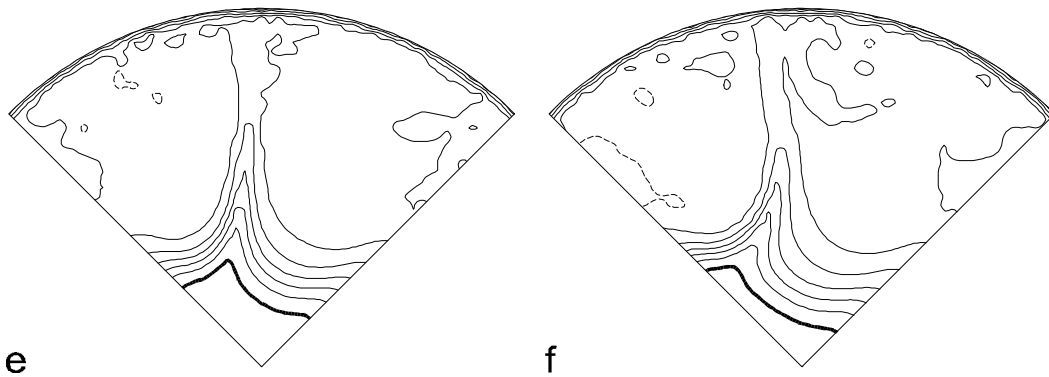
*figure 19     e. Case ri5; f. Case ri6*

*Different Marangoni numbers*

Various runs with different Marangoni numbers were performed for the convex container. In each of these calculations a = b = 0.5 and $N_{wG}$ = 31. Other parameter values are listed in section 3.4 and table 3. The results are discussed in section 3.6.

*Table 3.     Parameter values for runs with convex container.*

|          | Ma          | $N_\theta$ | $N_{wL}$ | $\Delta t$    | $N_t$ |
|----------|-------------|------------|----------|---------------|-------|
| Case r1  | $1\ 10^4$   | 60         | 60       | $5\ 10^{-4}$  | 4000  |
| Case r2  | $1\ 10^5$   | 60         | 60       | $5\ 10^{-4}$  | 4000  |
| Case r3  | $1\ 10^6$   | 60         | 60       | $5\ 10^{-4}$  | 4000  |
| Case r4  | $1\ 10^7$   | 60         | 60       | $5\ 10^{-4}$  | 4000  |
| Case r5  | $5\ 10^7$   | 150        | 90       | $5\ 10^{-5}$  | 4000  |

For the smaller grid, it was almost impossible to raise the Marangoni number further. For the larger grid (case r5), a higher Marangoni number was possible. However, for this run that covered only 40 real time seconds, $1.9\ 10^6$ CPU seconds on the Cray J90 were necessary.

Flow patterns and concentration distributions are depicted in the figures 20-24. The corresponding maximum interface velocities are depicted in figure 25.

*figure 20    Evolution of concentration field (left) and flowpattern (right) for the convex container, $H_L = H_G = 0.0141$ m. Case r1 ($Ma = 10^4$) after 400 seconds. $C_{max} = 0.99$; $\mathbf{D}_C = 0.04$; $\mathbf{D}_S = 1\ 10^{-10}$*



a



b

*figure 21    Evolution of concentration field (left) and flowpattern (right) for the convex container, $H_L = H_G = 0.0141$ m, case r2 ($Ma = 1\ 10^5$). For all plots $C_{max} = 0.99$; $\mathbf{D}_C = 0.04$; a. After 80 seconds; $\mathbf{D}_S = 1\ 10^{-4}$; b. After 200 seconds; $\mathbf{D}_S = 0.04$*
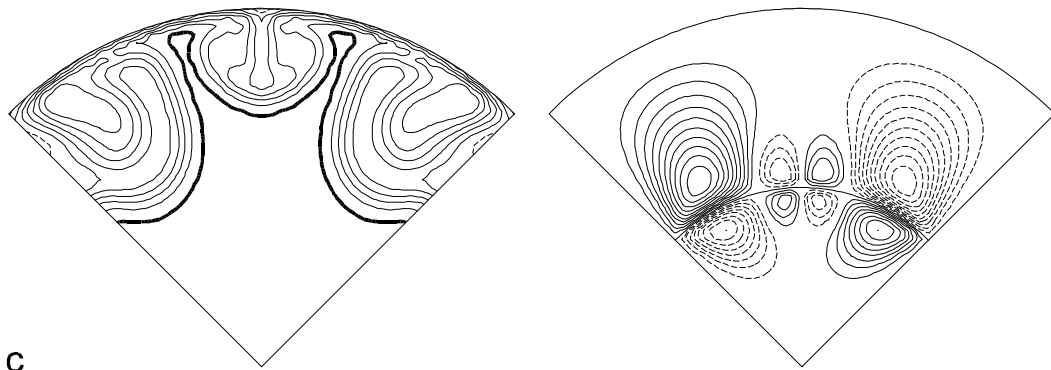
*figure 21    c. After 400 seconds; $D_S = 0.01$*
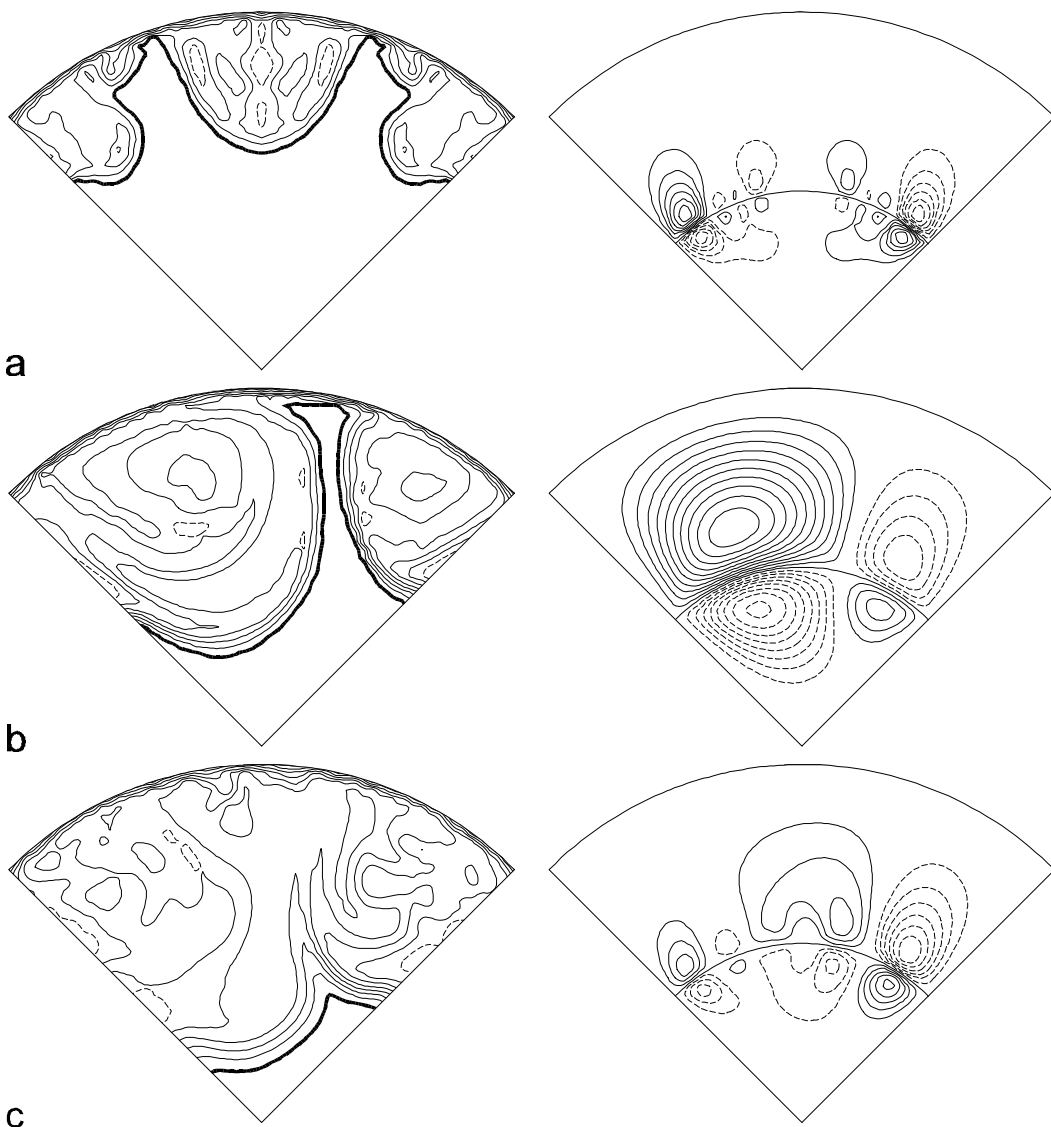


*figure 22    Evolution of concentration field (left) and flowpattern (right) for the convex container, $H_L = H_G = 0.0141$ m, case r3 (Ma = 1 10^6). For all plots $C_{max} = 0.99$; $D_C = 0.02$; a. After 80 seconds; $D_S = 0.04$; b. After 240 seconds; $D_S = 0.2$; c. After 400 seconds; $D_S = 0.1$*
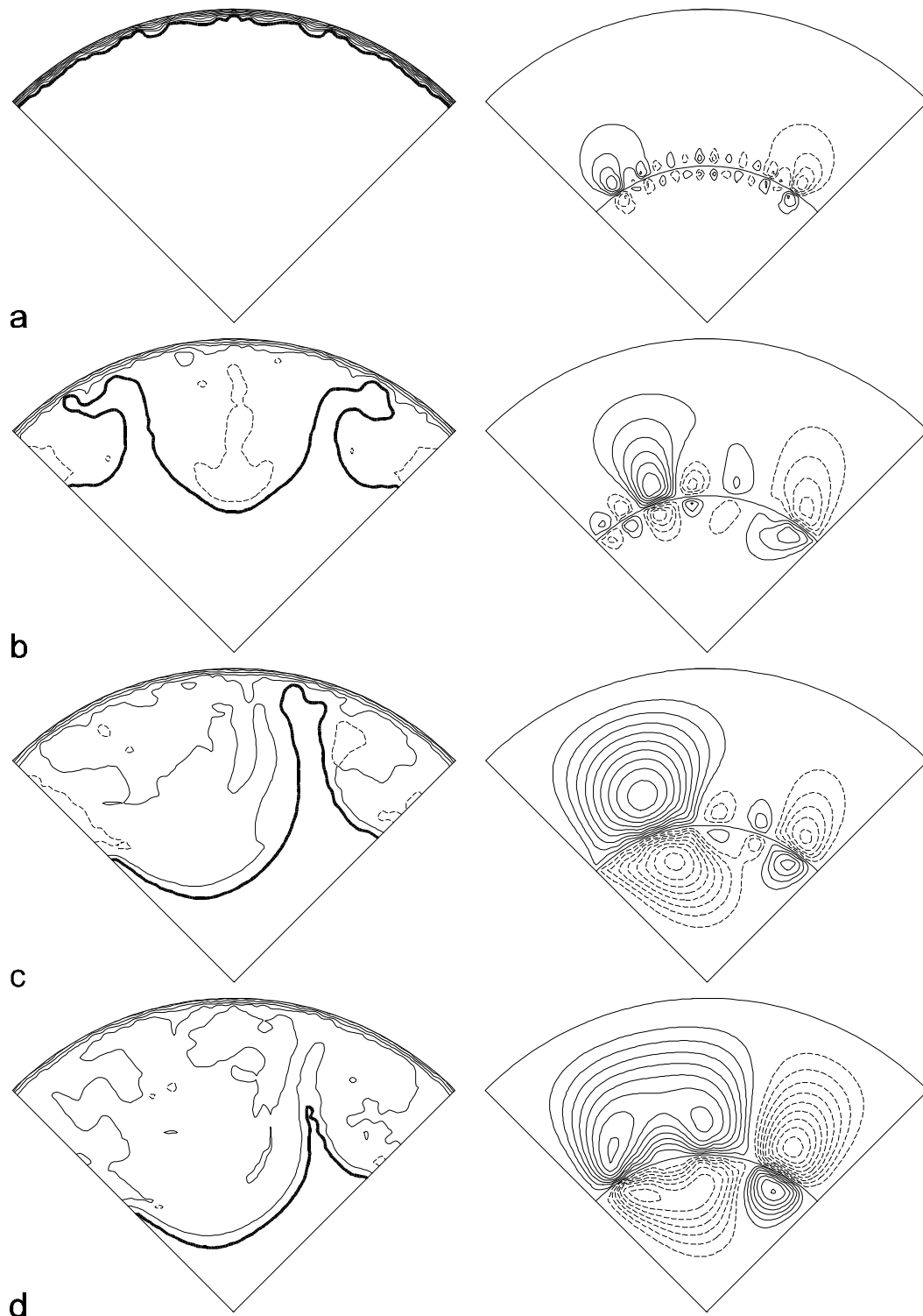
*figure 23    Evolution of concentration field (left) and flowpattern (right) for the convex container, $H_L = H_G = 0.0141$ m, case r4 (Ma = 1 $10^7$). For all plots $C_{max}$ = 0.99; $D_C$ = 0.02; $D_S$ = 0.2; a. After 4 seconds; b. After 40 seconds; c. After 80 seconds; d. After 120 seconds*
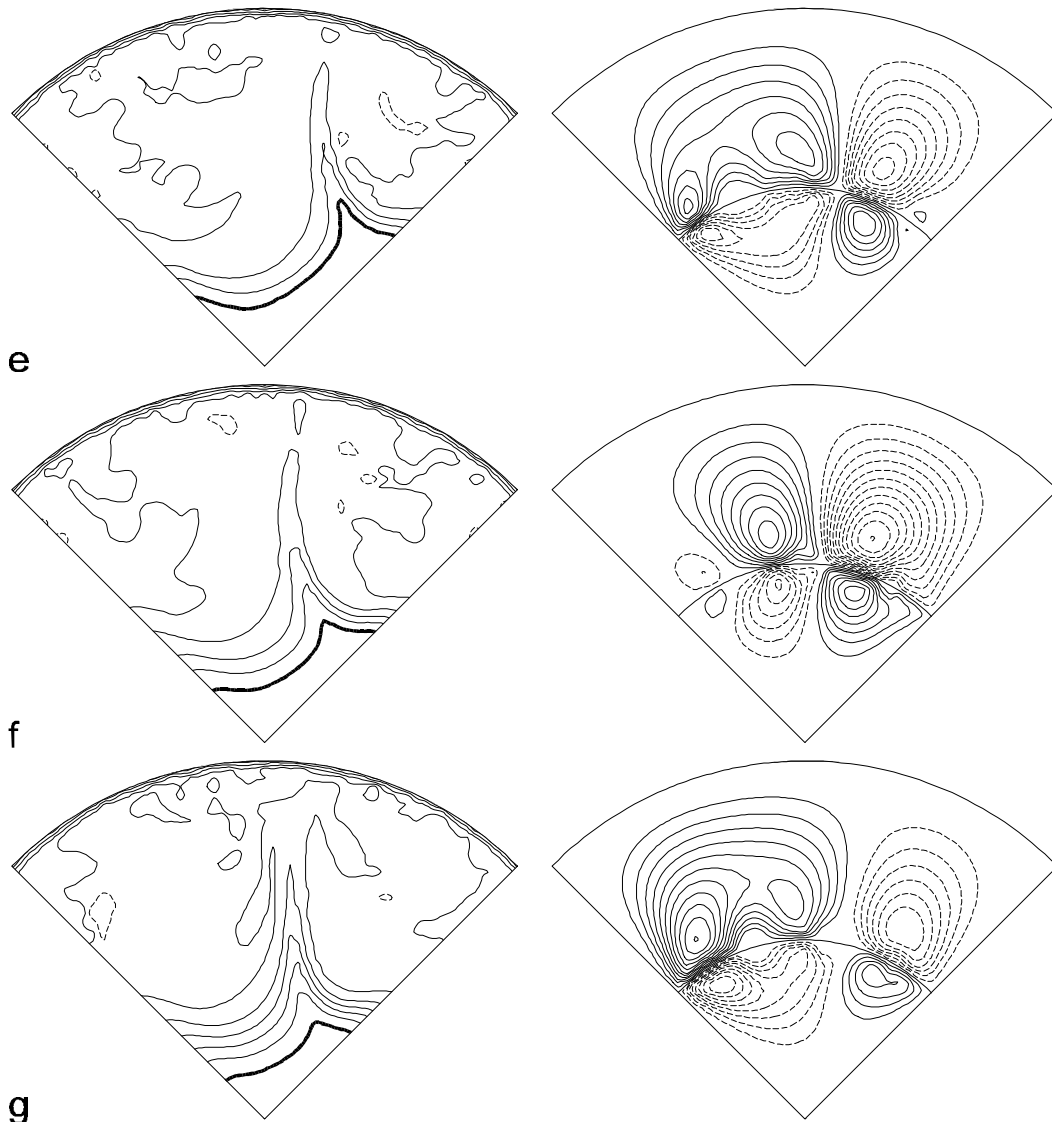
*figure 23     e. After 200 seconds; f. After 280 seconds; g. After 400 seconds*
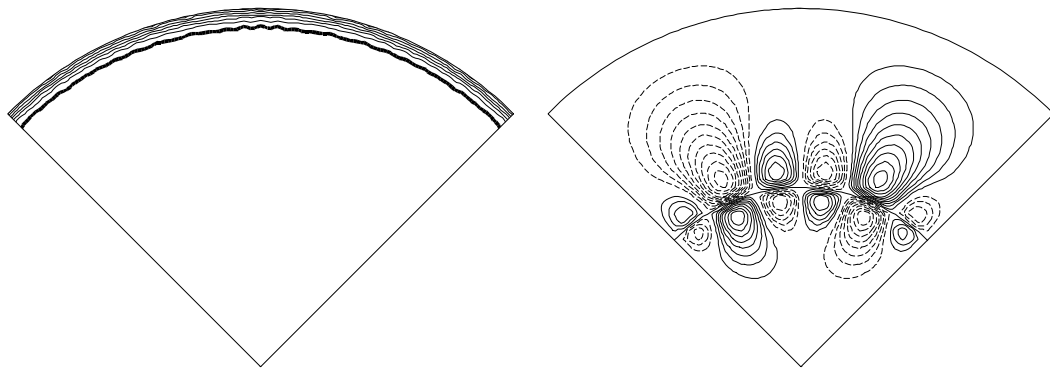


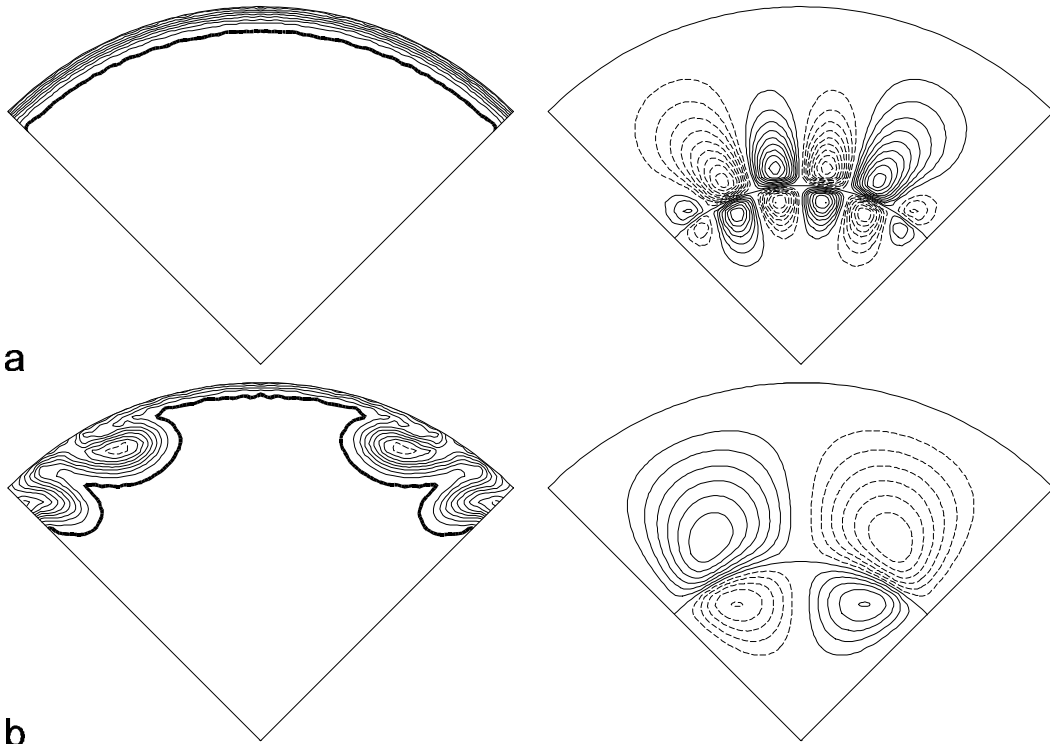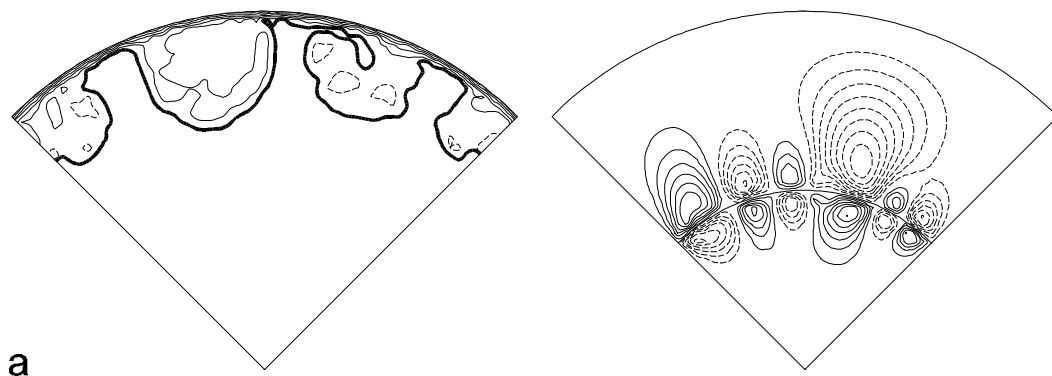*figure 24     Evolution of concentration field (left) and flowpattern (right) for the convex container, $H_L = H_G = 0.0141$ m, case r5 (Ma = 5 $10^7$). For all plots $C_{max} = 0.99$; $\mathbf{D}_C = 0.01$; a. After 12 seconds; $\mathbf{D}_S = 0.2$.*
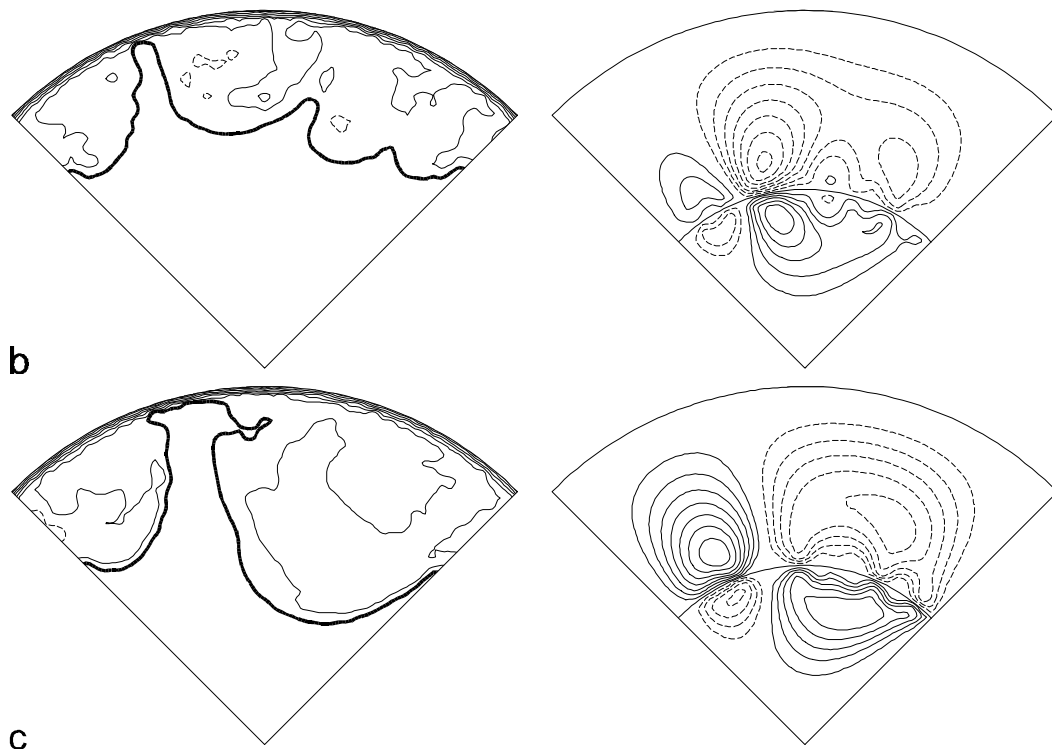
*figure 24    b. After 24 seconds; $\boldsymbol{D}_S$ = 0.4; c. After 40 seconds; $\boldsymbol{D}_S$ = 0.4*
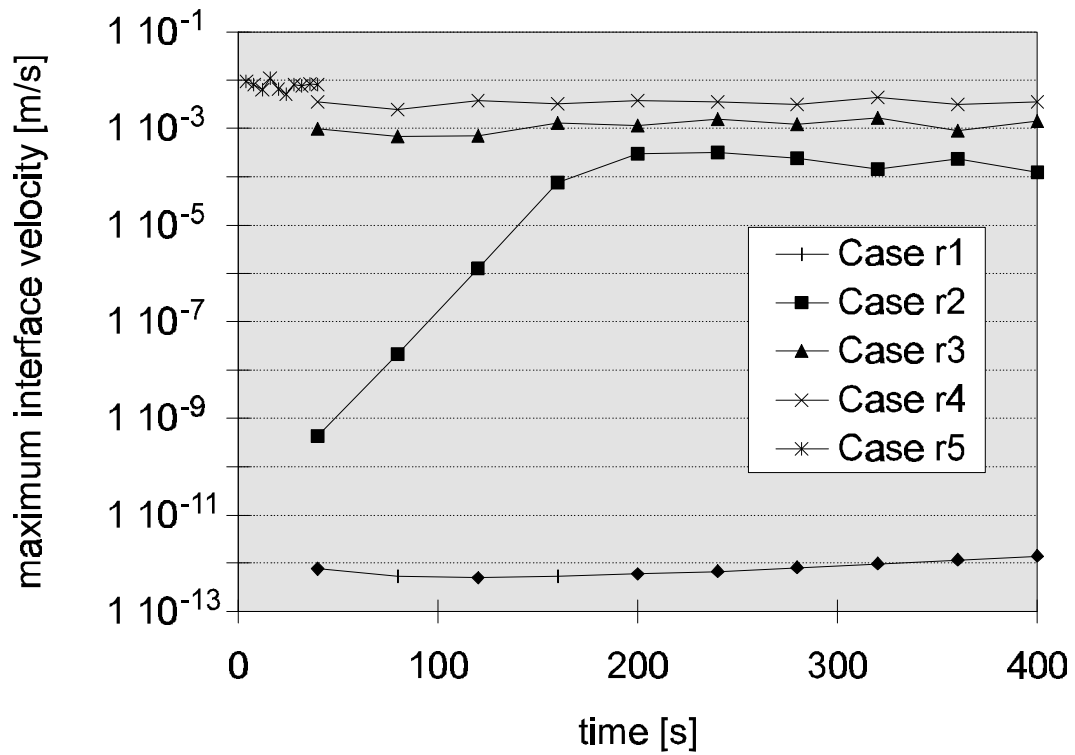


*figure 25    Maximum interface velocities in the convex container as a function of time.*

*Container 7*

One run was performed for the container 7, described in chapter 2. For this container, $N_P$ = 3 and $H_L$ = $H_G$ = 0.02 m. For this run, Ma = 2 $10^7$, $N_\theta$ = 90 and all other parameters equal to those described above. In figure 26, the evolution of the stream pattern and the concentration field are depicted for each 20 seconds.
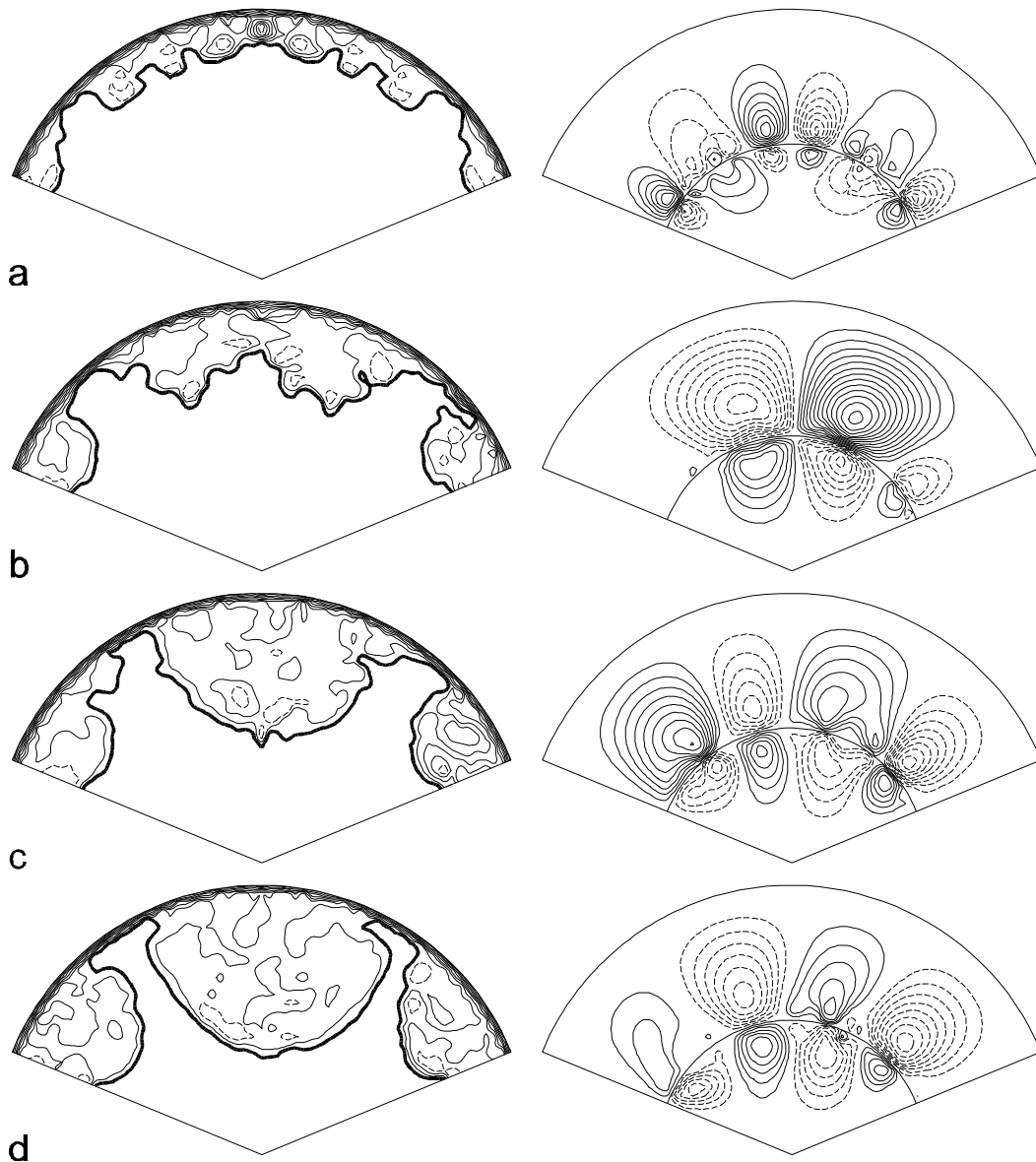


*figure 26*   *Evolution of concentration field (left) and flowpattern (right) for the case $N_P$ = 3, $H_L$ = $H_G$ = 0.02 m. For all iso concentration plots $\mathbf{D}_C$ = 0.01; $C_{max}$ = 0.99 a. After 20 seconds; $\mathbf{D}_S$ = 0.2; b. After 40 seconds; $\mathbf{D}_S$ = 0.4; c. After 60 seconds; $\mathbf{D}_S$ = 0.2; d. After 80 seconds; $\mathbf{D}_S$ = 0.2*
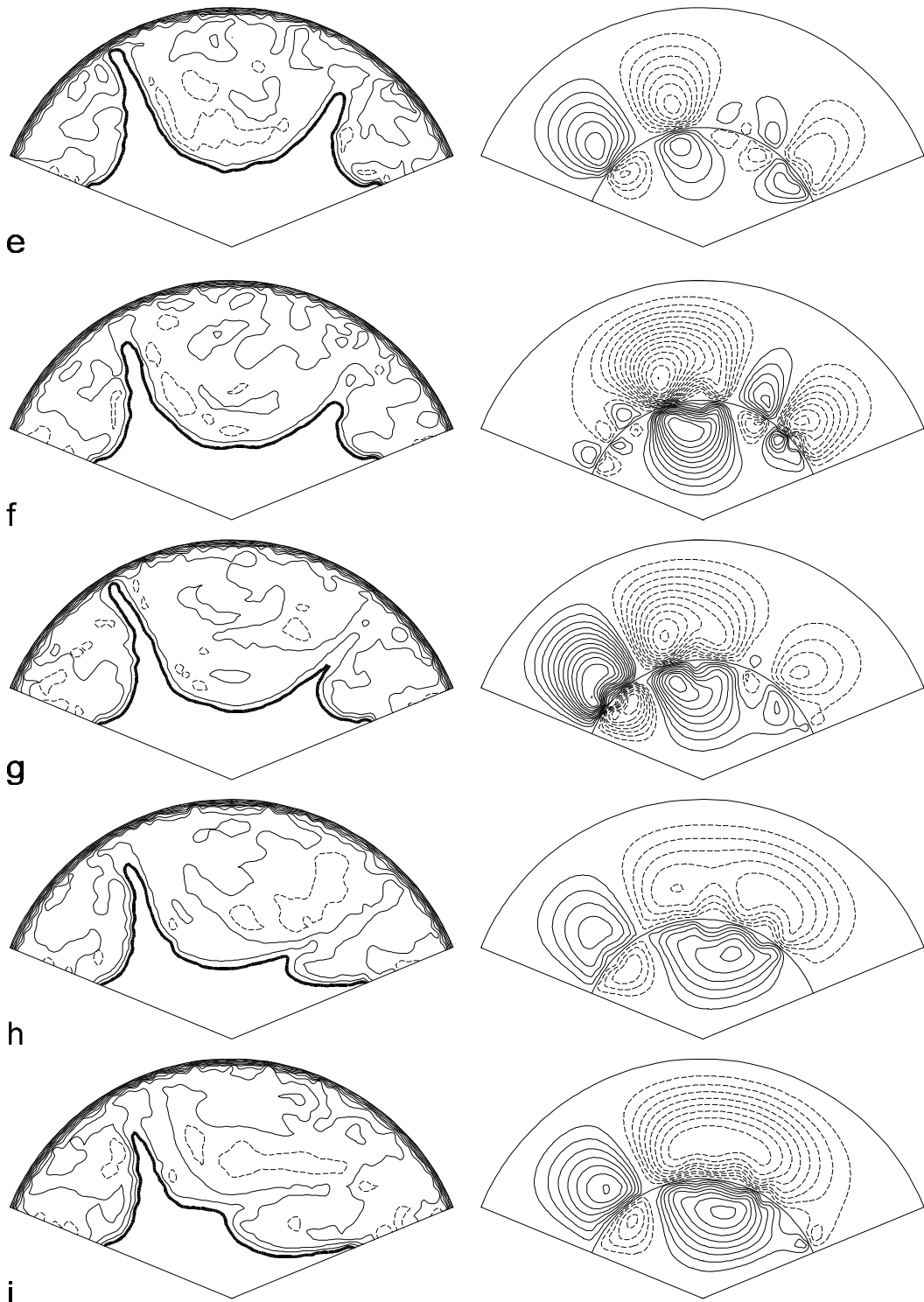
*figure 26*    *e. After 100 seconds $D_S$ = 0.4; f. After 120 seconds; $D_S$ = 0.2; g. After 140 seconds; $D_S$ = 0.2; h. After 160 seconds; $D_S$ = 0.4; i. After 180 seconds; $D_S$ = 0.4*

**j**
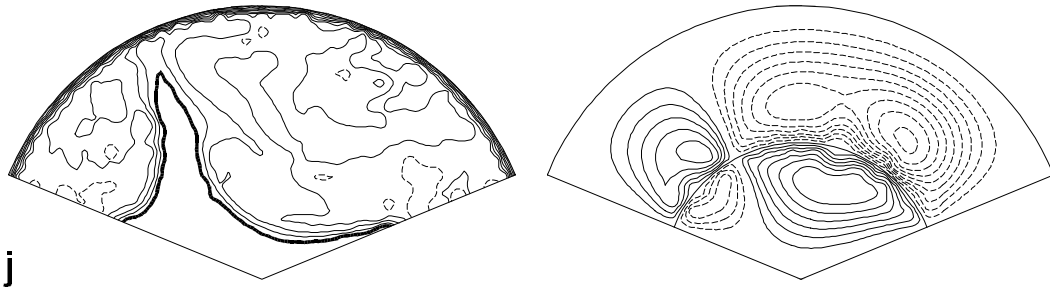
*figure 26*    *j. After 200 seconds; $D_S = 0.4$*

## 3.6    Discussion

The discussion of the results is focused on the comparison between the numerical and the experimental results. Furthermore, the influence of the Marangoni number on the numerical findings is contemplated, as well as the numerical peculiarities of the model.

*Flat container*

The numerical results indicate that the use of the experimental Marangoni number in the model leads to too high interface velocities and numerical problems. From figure 17, one can conclude that the results are quite sensitive to the values of a and b as well. The experimentally found maximum interface velocity for container 5 was in the order of 0.5 cm/s, which corresponds roughly to case 8, but case 4, 7 and 9 are close as well. When the concentration and flow patterns of these cases are studied, the following trend emerges.

Initially, a four roll cell pattern in the liquid evolves, which transforms into the two roll cell pattern which is experimentally observed. The higher the Marangoni number in the calculations, the shorter lasting the four roll cell period is. Although the flow pattern sometimes exhibits more than two roll cells after the transition to a two roll cell pattern, the base pattern consists of only two roll cells, which can be distinguished clearly from the concentration map. This qualitative picture corresponds quite well with the experiments, albeit that four roll cells have only been observed occasionally for a very short time, and not in the microgravity case. Furthermore, the numerically found concentration patterns show quite large gradients as a result of these four roll cells, and these have never been seen experimentally. The experimental concentration maps are much smoother during the entire experimental time.

Nevertheless, the overall numerical picture corresponds quite well to the experiments. There are a few reasons for the discussed discrepancy between the model and the experiments:

- The model represents a two-dimensional container without the sidewalls present in the three-dimensional experimental container. This renders the experimental velocities lower than the numerical ones. The three dimensional flow probably also helped to smooth out the concentration gradients.
- In the experiment, pollution was present in small quantities in the corners. The resulting concentration gradients have contributed to the formation of a two roll cell pattern (see

also chapter 2), but have also retarded the convection. Other dissimilarities between the perfect mathematical model and the experimental reality may also have played a role, such as a non-zero acetone concentration in the gas phase, non-uniform temperatures and meniscus effects.

- In the model, the interface is considered to be Newtonian and no surface excess quantities are taken into account. In reality, small traces of pollution easily retard interfacial movement by the Plateau-Marangoni-Gibbs effect. As long as not too much pollution is present, the omission of interfacial dilatational and shear viscosities is probably justified [15]. The exclusion of Gibbs absorption (of acetone) also introduces an error, both in the impulse as in the mass balance, as was demonstrated by Brian and Ross [16].

  All these omissions result in a too high velocity.

- Especially for higher Marangoni numbers, the model suffers from a lack of numerical accuracy that can only be compensated for by larger grids (setting a and b larger than 0.95 does not further increase accuracy substantially). Problems occur especially at the interface, where everything 'happens'. Larger grids, however, increase memory and CPU requirements drastically.

  Due to an inaccurate description of the mass transfer at the interface, concentration gradients may be too high or too low at the interface, even at low Marangoni numbers. Although wiggles have not been observed, other numerical disturbances are sometimes seen in the concentration maps (see figure 16) as a result of the high velocities. These disturbances can have influence on the roll cell pattern.

The model will be impossible to handle when all these omissions are included. Furthermore, the physical constants that govern for example the Plateau-Marangoni-Gibbs effect are largely unknown.

*Convex container*

When figures 15 of chapter 2 and figure 23 of this chapter (case r4) are compared, an accurate match is observed. In figure 23a, microconvection consisting of 16 roll cells is depicted. It should be kept in mind that this microconvective patterns is the result of an initial condition of six roll cells. In figure 23b these small roll cells have partly merged and from the concentration map a basic four roll cell pattern can be recognised. Then the two roll cell pattern emerges in figure 23c and remains stable for the remainder of the calculation time. Figures 23b, 23c and 23f compare very well to figures 15a, 15b and 15d of chapter 2, respectively. Quantitatively, the numerically calculated concentration gradients are a little bit larger than the experimentally found gradients. Also, the model results for container 7 are in quite good agreement with the experiments. In this case, figures 26c, 26f and 26i can be compared to figures 19b, 19c and 19d of chapter 2, respectively. Note that the experimental and numerical time to transit from the four roll cell to the two roll cell configuration are

approximately the same, 180 seconds. In the case of container 4 the experimental time is slightly shorter than the numerical one.

*Influence of the Marangoni number*

If the Marangoni number is increased for the flat container, the maximum interface velocity initially increases slightly more than proportionally. For higher Marangoni numbers, the increase becomes less than proportional (figure 17). For low Marangoni numbers, the flow only adjusts the concentration field marginally and the concentration gradient parallel to the interface is slightly increased with respect to the situation without flow. This slight increase in the concentration gradient can be observed when figures 8 and 9 are compared. For higher Marangoni numbers, the Marangoni effect progressively destroys the concentration gradient parallel to the interface.

For convex containers, the dependence of the maximum velocity on the Marangoni effect is slightly different (figure 25). For low Marangoni numbers (case r1), the numerical disturbance is not amplified and the flow is virtually non-existent. In the case of a flat container, the concentration gradient necessary for the Marangoni flow is provided for macroscopically. For $Ma = 10^4$, in the flat case, velocities are of the order $10^{-5}$ m/s while for the convex container the velocity is of the order $10^{-12}$ m/s. When Ma is raised to $10^5$, the numerical disturbance is amplified exponentially in time, which is clear from figure 25, case r2. (The exponential growth of the disturbance indicates that linear stability theory is applicable for these cases.) Clearly, besides the necessity of knowing the critical Marangoni number, knowledge about a critical time which is dependent on the Marangoni number is indispensable when the influence of the Marangoni effect on mass transfer needs to be described. For the Marangoni numbers employed in the microgravity experiments, this critical time is negligible small. For larger Marangoni numbers and times larger than the critical time, the dependence of the maximum interface velocity on Ma for convex containers is analogous to the dependence for the flat containers.

In some figures, it can be seen that a transition from a symmetrical concentration and flow pattern occurs to a chaotic pattern for larger Marangoni number and larger time. For $Ma = 10^6$, this transition can be nicely observed in figures 13 and 22. That is, for Marangoni numbers sufficiently large, the problem becomes sufficiently non-linear to make the solution of the problem asymmetrical.

*Numerical peculiarities*

The concentration maps depicted in some of the figures feature some disturbances, which can be assumed to be numerical. These disturbances have also influenced the flow pattern as they have triggered small roll cells disturbing the general flow pattern. In a sense, these numerical disturbances may simulate actual physical disturbances that are hard to model. The general numerical picture resembles the experimental picture quite well, so that it can be assumed that these numerical disturbances are no serious flaws in the model up to a certain

limit. For too high Marangoni numbers, too much of these physically unrealistic situations occur and moreover, at a certain point the numerical routine may fail to converge.


**3.7     Conclusions**

The model defined in this chapter represents the microgravity experiments quite well. The similarity is a little better for the convex container than for the flat container as the four roll cell pattern evident in the numerical simulations is hardly present in the experiments. The Marangoni number used for the simulations needs to be smaller than the experimental Marangoni number to get a good representation of the experiments. Some causes for the discrepancy between the model and the experiments have been proposed. The absence of the Plateau-Marangoni-Gibbs effect in the model is one of the most important ones.

The flat and convex containers have similar flow development. After a transition through a state with multiple roll cells (depending on the initial conditions and the container type), a four roll cell pattern evolves followed by a stable two roll cell pattern. A pattern with flow directed from the interface into the liquid along the solid side walls is selected preferentially.

The results of this work demonstrate that a representative part of the gas phase should be included in the model in order to obtain satisfactory results.

The numerical routine employed for this study renders much better results than routines employed in the past, which is mainly due to its complete implicity and the use of a preconditioning technique.

**List of symbols**

| | | |
|---|---|---|
| $a$ | grid refinement parameter introduced in equation (44) | [-] |
| $b$ | grid refinement parameter introduced in equation (45) | [-] |
| $Bi_N$ | Biot number defined by equation (**Fout! Bladwijzer niet gedefinieerd.**) | [-] |
| $Bi_R$ | Biot number defined by equation (62) | [-] |
| $c$ | concentration | [kg m$^{-3}$] or [-] |
| $C_{max}$ | maximum concentration contour line (used in figures) | [-] |
| $D$ | diffusion coefficient | [m$^2$ s$^{-1}$] |
| $H_G$ | size of gas phase (see figure 1 and 2) | [m] |
| $H_L$ | size of liquid phase (see figure 1 and 2) | [m] |
| $m$ | distribution coefficient (equation (12)) | [kg m$^{-3}$ kg$^{-1}$ m$^3$] |
| $Ma$ | Marangoni number | [-] |
| $N_{dist}$ | parameter defined by equation (60) | [-] |
| $N_P$ | integer, denoting size of convex container (figure 2) | [-] |
| $N_t$ | number of time steps | [-] |
| $N_{wG}$ | number of grid points in w-direction (gas phase) | [-] |
| $N_{wL}$ | number of grid points in w-direction (liquid phase) | [-] |
| $N_\eta$ | number of grid points in $\eta$-direction | [-] |

| $N_\theta$ | number of grid points in $\theta$-direction | [-] |
|---|---|---|
| r | radial co-ordinate | [m] or [-] |
| $R_G$ | gas phase mass transfer resistance (equation (62)) | [-] |
| Sc | Schmidt number defined by equation (24) | [-] |
| t | time | [s] or [-] |
| u | horizontal velocity | [m s$^{-1}$] or [-] |
| v | vertical velocity | [m s$^{-1}$] or [-] |
| Vi | viscosity ratio defined by equation (25) | [-] |
| x | length co-ordinate | [m] or [-] |
| $X_{dist}$ | parameter defined by equation (60) | [-] |
| y | length co-ordinate | [m] or [-] |
| w | length co-ordinate defined by equations (42) and (43) | [-] |
| z | length co-ordinate defined by figure 3 | [-] |
| $z_T$ | parameter defined by figure 3 | [-] |
| $\gamma$ | surface tension | [N m$^{-1}$] |
| $\Delta_C$ | distance between concentration contour lines (figures) | [-] |
| $\Delta_S$ | distance between stream function contour lines (figures) | [-] |
| $\varepsilon$ | parameter defined by figure 3 | [-] |
| $\eta$ | co-ordinate defined by figure 3 | [-] |
| $\theta$ | angular co-ordinate | [rad] |
| $\mu$ | dynamic viscosity | [Pa s] |
| $\nu$ | kinematic viscosity | [m$^2$ s$^{-1}$] |
| $\psi$ | stream function | [m$^2$ s$^{-1}$] or [-] |
| $\omega$ | vorticity | [s$^{-1}$] or [-] |

*Subscripts*

| G | gas phase |
|---|---|
| i | interface |
| L | liquid phase |
| P | phase (gas or liquid) |
| $\Gamma$ | parallel to the interface |
| 0 | initial |

## Literature

[1]   H.W. Hoogstraten, H.C.J. Hoefsloot, L.P.B.M. Janssen, "Marangoni convection in V-shaped containers", J. Eng. Math., 26, 21-37, 1992

[2]   R. Peyret, T.D. Taylor, "Computational methods for fluid flow", Springer-Verlag, New York, 1983

[3]   A. van der Ploeg, "Preconditioning for sparse matrices with applications", Ph.D. Thesis University of Groningen, 1994

[4]   H.A. Dijkstra, "Mass transfer induced convection near gas-liquid interfaces", Ph.D. Thesis University of Groningen, 1988

[5]   H.A. Dijkstra, A.I. van de Vooren, "Initial flow development due to Marangoni convection in a mass transfer system", Int. J. Heat Mass Transfer, 28(12), 2315-2322, 1985

[6]   E. Evren-Salamet, V.S. Arpaci, A.T. Chai, "Thermocapillary-driven flow past the Marangoni instability", Numerical Heat Transfer, Part A, 26, 521-535, 1994

[7]   H.C.J. Hoefsloot, L.P.B.M. Janssen, H.W. Hoogstraten, "Marangoni convection around a ventilated air bubble under microgravity conditions", Chem. Eng. Sci., 49(1), 29-39, 1994

[8]   I.B. Simanovskii, A.A. Nepomnyashchy, "Convective instabilities in systems with interface", Gordon and Breach, Singapore, 1993

[9]   C.V. Sternling, L.E. Scriven, "Interfacial turbulence: hydrodynamic instability and the Marangoni effect", A.I.Ch.E. J., 5(4), 514-523, 1959

[10]  S. Yasuhiro, T. Sato, N. Imaishi, A. Hirata, M. Kumagawa, "Numerical simulation of solutal Marangoni convection during liquid mixing under microgravity", Microgravity Sci. Technol. IX/4, 237-244, 1996

[11]  H.W. van der Klooster, "The influence of gradients in surface tension on the mass transfer in gas liquid systems", Ph.D. thesis, University of Groningen, 1978

[12]  L.P.B.M. Janssen, M.M.C.G. Warmoeskerken, "Transport phenomena data companion", Edward Arnold, London, 1987

[13]  J.H. Lichtenbelt, B.J. Schram, "Vapor-liquid equilibrium of water-acetone air at ambient temperatures and pressures. An analysis of different VLE-fitting methods", Ind. Eng. Chem. Process Des. Dev., 24, 391-397, 1985

[14]  International Critical Tables of Numerical Data, Physics, Chemistry and Technology, IV, McGraw-Hill, New York, 1928

[15]  J.C. Berg, A. Acrivos, "The effect of surface active agents on convection cells induced by surface tension", Chem. Eng. Sci., 20, 737-745, 1965

[16]  P.L.T. Brian, J.R. Ross, "The effect of Gibbs adsorption on Marangoni instability in penetration mass transfer", A.I.Ch.E. J., 18(3), 582-591, 1972

## Appendix A

In this appendix, the discretised versions of the governing equations are presented.

*Flat container*

The Navier Stokes equation:

$$\omega_{i-1,j+1}^{n+1}\left\{\frac{\text{Vi}_P\,\Omega3_{i,j}}{8\Delta w_P\Delta\eta}\right\}+\omega_{i+1,j+1}^{n+1}\left\{\frac{-\text{Vi}_P\,\Omega3_{i,j}}{8\Delta w_P\Delta\eta}\right\}+\omega_{i,j}^{n+1}\left\{\frac{1}{\Delta t}+\frac{\text{Vi}_P\,\Omega2_{i,j}}{(\Delta\eta)^2}+\frac{\text{Vi}_P\,\Omega4_j}{(\Delta w_P)^2}\right\}$$

$$\omega_{i,j+1}^{n+1}\left\{\frac{\Omega1_j\left(\psi_{i+1,j+1}^{n+1}-\psi_{i-1,j+1}^{n+1}\right)}{16\Delta w_P\Delta\eta}+\frac{\Omega1_j\left(\psi_{i+1,j+1}^{n}-\psi_{i-1,j+1}^{n}\right)}{16\Delta w_P\Delta\eta}-\frac{\text{Vi}_P\,\Omega4_j}{2(\Delta w_P)^2}-\frac{\text{Vi}_P\,\Omega6_j}{4\Delta w_P}\right\}+$$

$$\omega_{i-1,j}^{n+1}\left\{\frac{\Omega1_j\left(\psi_{i-1,j+1}^{n+1}-\psi_{i-1,j-1}^{n+1}\right)}{16\Delta w_P\Delta\eta}+\frac{\Omega1_j\left(\psi_{i-1,j+1}^{n}-\psi_{i-1,j-1}^{n}\right)}{16\Delta w_P\Delta\eta}-\frac{\text{Vi}_P\,\Omega2_{i,j}}{2(\Delta\eta)^2}+\frac{\text{Vi}_P\,\Omega5_{i,j}}{4\Delta\eta}\right\}+$$

$$\omega_{i+1,j}^{n+1}\left\{\frac{-\Omega1_j\left(\psi_{i+1,j+1}^{n+1}-\psi_{i+1,j-1}^{n+1}\right)}{16\Delta w_P\Delta\eta}+\frac{-\Omega1_j\left(\psi_{i+1,j+1}^{n}-\psi_{i+1,j-1}^{n}\right)}{16\Delta w_P\Delta\eta}-\frac{\text{Vi}_P\,\Omega2_{i,j}}{2(\Delta\eta)^2}-\frac{\text{Vi}_P\,\Omega5_{i,j}}{4\Delta\eta}\right\}+$$

$$\omega_{i,j-1}^{n+1}\left\{\frac{-\Omega1_j\left(\psi_{i+1,j-1}^{n+1}-\psi_{i-1,j-1}^{n+1}\right)}{16\Delta w_P\Delta\eta}+\frac{-\Omega1_j\left(\psi_{i+1,j-1}^{n}-\psi_{i-1,j-1}^{n}\right)}{16\Delta w_P\Delta\eta}-\frac{\text{Vi}_P\,\Omega4_j}{2(\Delta w_P)^2}+\frac{\text{Vi}_P\,\Omega6_j}{4\Delta w_P}\right\}+$$

$$\omega_{i-1,j-1}^{n+1}\left\{\frac{-\text{Vi}_P\,\Omega3_{i,j}}{8\Delta w_P\Delta\eta}\right\}+\psi_{i-1,j-1}^{n+1}\left\{\frac{\Omega1_j\left(\omega_{i,j-1}^{n+1}-\omega_{i-1,j}^{n+1}\right)}{16\Delta w_P\Delta\eta}\right\}+\psi_{i-1,j+1}^{n+1}\left\{\frac{\Omega1_j\left(\omega_{i-1,j}^{n+1}-\omega_{i,j+1}^{n+1}\right)}{16\Delta w_P\Delta\eta}\right\}+$$

$$\omega_{i+1,j-1}^{n+1}\left\{\frac{\text{Vi}_P\,\Omega3_{i,j}}{8\Delta w_P\Delta\eta}\right\}+\psi_{i+1,j+1}^{n+1}\left\{\frac{\Omega1_j\left(\omega_{i,j+1}^{n+1}-\omega_{i+1,j}^{n+1}\right)}{16\Delta w_P\Delta\eta}\right\}+\psi_{i+1,j-1}^{n+1}\left\{\frac{\Omega1_j\left(\omega_{i+1,j}^{n+1}-\omega_{i,j-1}^{n+1}\right)}{16\Delta w_P\Delta\eta}\right\}=$$

$$\omega_{i-1,j+1}^{n}\left\{\frac{-\text{Vi}_P\,\Omega3_{i,j}}{8\Delta w_P\Delta\eta}\right\}+\omega_{i,j+1}^{n}\left\{\frac{-\Omega1_j\left(\psi_{i+1,j+1}^{n}-\psi_{i-1,j+1}^{n}\right)}{16\Delta w_P\Delta\eta}+\frac{\text{Vi}_P\,\Omega4_j}{2(\Delta w_P)^2}+\frac{\text{Vi}_P\,\Omega6_j}{4\Delta w_P}\right\}+$$

$$\omega_{i+1,j+1}^{n}\left\{\frac{\text{Vi}_P\,\Omega3_{i,j}}{8\Delta w_P\Delta\eta}\right\}+\omega_{i-1,j}^{n}\left\{\frac{-\Omega1_j\left(\psi_{i-1,j+1}^{n}-\psi_{i-1,j-1}^{n}\right)}{16\Delta w_P\Delta\eta}+\frac{\text{Vi}_P\,\Omega2_{i,j}}{2(\Delta\eta)^2}-\frac{\text{Vi}_P\,\Omega5_{i,j}}{4\Delta\eta}\right\}+$$

$$\omega_{i,j}^{n}\left\{\frac{1}{\Delta t}-\frac{\text{Vi}_P\,\Omega2_{i,j}}{(\Delta\eta)^2}-\frac{\text{Vi}_P\,\Omega4_j}{(\Delta w_P)^2}\right\}+\omega_{i-1,j-1}^{n}\left\{\frac{\text{Vi}_P\,\Omega3_{i,j}}{8\Delta w_P\Delta\eta}\right\}+\omega_{i+1,j-1}^{n}\left\{\frac{-\text{Vi}_P\,\Omega3_{i,j}}{8\Delta w_P\Delta\eta}\right\}$$

$$\omega_{i+1,j}^{n}\left\{\frac{\Omega1_j\left(\psi_{i+1,j+1}^{n}-\psi_{i+1,j-1}^{n}\right)}{16\Delta w_P\Delta\eta}+\frac{\text{Vi}_P\,\Omega2_{i,j}}{2(\Delta\eta)^2}+\frac{\text{Vi}_P\,\Omega5_{i,j}}{4\Delta\eta}\right\}+$$

$$\omega_{i,j-1}^{n}\left\{\frac{\Omega1_j\left(\psi_{i+1,j-1}^{n}-\psi_{i-1,j-1}^{n}\right)}{16\Delta w_P\Delta\eta}+\frac{\text{Vi}_P\,\Omega4_j}{2(\Delta w_P)^2}-\frac{\text{Vi}_P\,\Omega6_j}{4\Delta w_P}\right\} \tag{A.1}$$

In the next equations f is either f or g, depending on the phase P.

$$\Omega 1_j = \frac{1}{f'(w_j)(1-\varepsilon)\big(\varepsilon + f(w_j)(1-\varepsilon)\big)}\Bigg|_P \tag{A.2}$$

$$\Omega 2_{i,j} = \frac{1+\eta_i^2}{\big(\varepsilon + f(w_j)(1-\varepsilon)\big)^2}\Bigg|_P \tag{A.3}$$

$$\Omega 3_{i,j} = \frac{-2\eta_i}{f'(w_j)(1-\varepsilon)\big(\varepsilon + f(w_j)(1-\varepsilon)\big)}\Bigg|_P \tag{A.4}$$

$$\Omega 4_j = \left(\frac{1}{f'(w_j)(1-\varepsilon)}\right)^2\Bigg|_P \tag{A.5}$$

$$\Omega 5_{i,j} = \frac{2\eta_i}{\big(\varepsilon + f(w_j)(1-\varepsilon)\big)^2}\Bigg|_P \tag{A.6}$$

$$\Omega 6_j = -\frac{1}{(1-\varepsilon)^2}\frac{f''(w)}{f'(w)^3}\Bigg|_P \tag{A.7}$$

The continuity equation:

$$\omega_{i,j}^{n+1} + \psi_{i-1,j+1}^{n+1}\left\{\frac{-\Omega 3_{i,j}}{4\Delta w_P \Delta\eta}\right\} + \psi_{i,j+1}^{n+1}\left\{\frac{\Omega 4_j}{(\Delta w_P)^2} + \frac{\Omega 6_j}{2\Delta w_P}\right\} + \psi_{i+1,j+1}^{n+1}\left\{\frac{\Omega 3_{i,j}}{4\Delta w_P \Delta\eta}\right\} +$$

$$\psi_{i-1,j}^{n+1}\left\{\frac{\Omega 2_{i,j}}{(\Delta\eta)^2} - \frac{\Omega 5_{i,j}}{2\Delta\eta}\right\} + \psi_{i,j}^{n+1}\left\{-\frac{2\cdot\Omega 2_{i,j}}{(\Delta\eta)^2} - \frac{2\cdot\Omega 4_j}{(\Delta w_P)^2}\right\} + \psi_{i+1,j}^{n+1}\left\{\frac{\Omega 2_{i,j}}{(\Delta\eta)^2} + \frac{\Omega 5_{i,j}}{2\Delta\eta}\right\} +$$

$$\psi_{i-1,j-1}^{n+1}\left\{\frac{\Omega 3_{i,j}}{4\Delta w_P \Delta\eta}\right\} + \psi_{i,j-1}^{n+1}\left\{\frac{\Omega 4_j}{(\Delta w_P)^2} - \frac{\Omega 6_j}{2\Delta w_P}\right\} + \psi_{i+1,j-1}^{n+1}\left\{\frac{-\Omega 3_{i,j}}{4\Delta w_P \Delta\eta}\right\} = 0$$

$$\tag{A.8}$$

The convection-diffusion equation:

$$
c_{i-1,j+1}^{n+1}\left\{\frac{\Omega3_{i,j}}{8Sc_P\Delta w_P\Delta\eta}\right\} + c_{i+1,j+1}^{n+1}\left\{\frac{-\Omega3_{i,j}}{8Sc_P\Delta w_P\Delta\eta}\right\} + c_{i,j}^{n+1}\left\{\frac{1}{\Delta t} + \frac{\Omega2_{i,j}}{Sc_P(\Delta\eta)^2} + \frac{\Omega4_j}{Sc_P(\Delta w_P)^2}\right\} +
$$

$$
c_{i,j+1}^{n+1}\left\{\frac{\Omega1_j\left(\psi_{i+1,j+1}^{n+1} - \psi_{i-1,j+1}^{n+1}\right)}{16\Delta w_P\Delta\eta} + \frac{\Omega1_j\left(\psi_{i+1,j+1}^{n} - \psi_{i-1,j+1}^{n}\right)}{16\Delta w_P\Delta\eta} - \frac{\Omega4_j}{2Sc_P(\Delta w_P)^2} - \frac{\Omega6_j}{4Sc_P\Delta w_P}\right\} +
$$

$$
+c_{i-1,j}^{n+1}\left\{\frac{\Omega1_j\left(\psi_{i-1,j+1}^{n+1} - \psi_{i-1,j-1}^{n+1}\right)}{16\Delta w_P\Delta\eta} + \frac{\Omega1_j\left(\psi_{i-1,j+1}^{n} - \psi_{i-1,j-1}^{n}\right)}{16\Delta w_P\Delta\eta} - \frac{\Omega2_{i,j}}{2Sc_P(\Delta\eta)^2} + \frac{\Omega5_{i,j}}{4Sc_P\Delta\eta}\right\} +
$$

$$
c_{i+1,j}^{n+1}\left\{\frac{-\Omega1_j\left(\psi_{i+1,j+1}^{n+1} - \psi_{i+1,j-1}^{n+1}\right)}{16\Delta w_P\Delta\eta} + \frac{-\Omega1_j\left(\psi_{i+1,j+1}^{n} - \psi_{i+1,j-1}^{n}\right)}{16\Delta w_P\Delta\eta} - \frac{\Omega2_{i,j}}{2Sc_P(\Delta\eta)^2} - \frac{\Omega5_{i,j}}{4Sc_P\Delta\eta}\right\} +
$$

$$
c_{i,j-1}^{n+1}\left\{\frac{-\Omega1_j\left(\psi_{i+1,j-1}^{n+1} - \psi_{i-1,j-1}^{n+1}\right)}{16\Delta w_P\Delta\eta} + \frac{-\Omega1_j\left(\psi_{i+1,j-1}^{n} - \psi_{i-1,j-1}^{n}\right)}{16\Delta w_P\Delta\eta} - \frac{\Omega4_j}{2Sc_P(\Delta w_P)^2} + \frac{\Omega6_j}{4Sc_P\Delta w_P}\right\} +
$$

$$
c_{i+1,j-1}^{n+1}\left\{\frac{\Omega3_{i,j}}{8Sc_P\Delta w_P\Delta\eta}\right\} + \psi_{i-1,j-1}^{n+1}\left\{\frac{\Omega1_j\left(c_{i,j-1}^{n+1} - c_{i-1,j}^{n+1}\right)}{16\Delta w_P\Delta\eta}\right\} + \psi_{i-1,j+1}^{n+1}\left\{\frac{\Omega1_j\left(c_{i-1,j}^{n+1} - c_{i,j+1}^{n+1}\right)}{16\Delta w_P\Delta\eta}\right\} +
$$

$$
c_{i-1,j-1}^{n+1}\left\{\frac{-\Omega3_{i,j}}{8Sc_P\Delta w_P\Delta\eta}\right\} + +\psi_{i+1,j+1}^{n+1}\left\{\frac{\Omega1_j\left(c_{i,j+1}^{n+1} - c_{i+1,j}^{n+1}\right)}{16\Delta w_P\Delta\eta}\right\} + \psi_{i+1,j-1}^{n+1}\left\{\frac{\Omega1_j\left(c_{i+1,j}^{n+1} - c_{i,j-1}^{n+1}\right)}{16\Delta w_P\Delta\eta}\right\} =
$$

$$
c_{i-1,j+1}^{n}\left\{\frac{-\Omega3_{i,j}}{8Sc_P\Delta w_P\Delta\eta}\right\} + c_{i,j+1}^{n}\left\{\frac{-\Omega1_j\left(\psi_{i+1,j+1}^{n} - \psi_{i-1,j+1}^{n}\right)}{16\Delta w_P\Delta\eta} + \frac{\Omega4_j}{2Sc_P(\Delta w_P)^2} + \frac{\Omega6_j}{4Sc_P\Delta w_P}\right\} +
$$

$$
c_{i+1,j+1}^{n}\left\{\frac{\Omega3_{i,j}}{8Sc_P\Delta w_P\Delta\eta}\right\} + c_{i-1,j}^{n}\left\{\frac{-\Omega1_j\left(\psi_{i-1,j+1}^{n} - \psi_{i-1,j-1}^{n}\right)}{16\Delta w_P\Delta\eta} + \frac{\Omega2_{i,j}}{2Sc_P(\Delta\eta)^2} - \frac{\Omega5_{i,j}}{4Sc_P\Delta\eta}\right\} +
$$

$$
c_{i,j}^{n}\left\{\frac{1}{\Delta t} - \frac{\Omega2_{i,j}}{Sc_P(\Delta\eta)^2} - \frac{\Omega4_j}{Sc_P(\Delta w_P)^2}\right\} +
$$

$$
c_{i+1,j}^{n}\left\{\frac{\Omega1_j\left(\psi_{i+1,j+1}^{n} - \psi_{i+1,j-1}^{n}\right)}{16\Delta w_P\Delta\eta} + \frac{\Omega2_{i,j}}{2Sc_P(\Delta\eta)^2} + \frac{\Omega5_{i,j}}{4Sc_P\Delta\eta}\right\} + c_{i-1,j-1}^{n}\left\{\frac{\Omega3_{i,j}}{8Sc_P\Delta w_P\Delta\eta}\right\} +
$$

$$
c_{i,j-1}^{n}\left\{\frac{\Omega1_j\left(\psi_{i+1,j-1}^{n} - \psi_{i-1,j-1}^{n}\right)}{16\Delta w_P\Delta\eta} + \frac{\Omega4_j}{2Sc_P(\Delta w_P)^2} - \frac{\Omega6_j}{4Sc_P\Delta w_P}\right\} + c_{i+1,j-1}^{n}\left\{\frac{-\Omega3_{i,j}}{8Sc_P\Delta w_P\Delta\eta}\right\}
$$

$$
(A.9)
$$

*Convex container*

Navier-Stokes equation:

$$\omega_{i,j+1}^{n+1}\left\{\frac{-\Omega1_j\left(\psi_{i+1,j+1}^{n+1}-\psi_{i-1,j+1}^{n+1}\right)}{16\Delta w_P\Delta\theta}+\frac{-\Omega1_j\left(\psi_{i+1,j+1}^{n}-\psi_{i-1,j+1}^{n}\right)}{16\Delta w_P\Delta\theta}-\frac{Vi_P\Omega3_j}{2\left(\Delta w_P\right)^2}-\frac{Vi_P\Omega4_j}{4\Delta w_P}\right\}+$$

$$\omega_{i-1,j}^{n+1}\left\{\frac{-\Omega1_j\left(\psi_{i-1,j+1}^{n+1}-\psi_{i-1,j-1}^{n+1}\right)}{16\Delta w_P\Delta\theta}+\frac{-\Omega1_j\left(\psi_{i-1,j+1}^{n}-\psi_{i-1,j-1}^{n}\right)}{16\Delta w_P\Delta\theta}-\frac{Vi_P\Omega2_j}{2\left(\Delta\theta\right)^2}\right\}+$$

$$\omega_{i+1,j}^{n+1}\left\{\frac{\Omega1_j\left(\psi_{i+1,j+1}^{n+1}-\psi_{i+1,j-1}^{n+1}\right)}{16\Delta w_P\Delta\theta}+\frac{\Omega1_j\left(\psi_{i+1,j+1}^{n}-\psi_{i+1,j-1}^{n}\right)}{16\Delta w_P\Delta\theta}-\frac{Vi_P\Omega2_j}{2\left(\Delta\theta\right)^2}\right\}+$$

$$\omega_{i,j-1}^{n+1}\left\{\frac{\Omega1_j\left(\psi_{i+1,j-1}^{n+1}-\psi_{i-1,j-1}^{n+1}\right)}{16\Delta w_P\Delta\theta}+\frac{\Omega1_j\left(\psi_{i+1,j-1}^{n}-\psi_{i-1,j-1}^{n}\right)}{16\Delta w_P\Delta\theta}-\frac{Vi_P\Omega3_j}{2\left(\Delta w_P\right)^2}+\frac{Vi_P\Omega4_j}{4\Delta w_P}\right\}+$$

$$\omega_{i,j}^{n+1}\left\{\frac{1}{\Delta t}+\frac{Vi_P\Omega2_j}{\left(\Delta\theta\right)^2}+\frac{Vi_P\Omega3_j}{\left(\Delta w_P\right)^2}\right\}+\psi_{i-1,j+1}^{n+1}\left\{\frac{\Omega1_j\left(\omega_{i,j+1}^{n}-\omega_{i-1,j}^{n}\right)}{16\Delta w_P\Delta\theta}\right\}+$$

$$\psi_{i+1,j+1}^{n+1}\left\{\frac{\Omega1_j\left(\omega_{i+1,j}^{n}-\omega_{i,j+1}^{n}\right)}{16\Delta w_P\Delta\theta}\right\}+\psi_{i-1,j-1}^{n+1}\left\{\frac{\Omega1_j\left(\omega_{i-1,j}^{n}-\omega_{i,j-1}^{n}\right)}{16\Delta w_P\Delta\theta}\right\}+$$

$$\psi_{i+1,j-1}^{n+1}\left\{\frac{\Omega1_j\left(\omega_{i,j-1}^{n}-\omega_{i+1,j}^{n}\right)}{16\Delta w_P\Delta\theta}\right\}=\omega_{i,j+1}^{n}\left\{\frac{\Omega1_j\left(\psi_{i+1,j+1}^{n}-\psi_{i-1,j+1}^{n}\right)}{16\Delta w_P\Delta\theta}+\frac{Vi_P\Omega3_j}{2\left(\Delta w_P\right)^2}+\frac{Vi_P\Omega4_j}{4\Delta w_P}\right\}+$$

$$\omega_{i-1,j}^{n}\left\{\frac{\Omega1_j\left(\psi_{i-1,j+1}^{n}-\psi_{i-1,j-1}^{n}\right)}{16\Delta w_P\Delta\theta}+\frac{Vi_P\Omega2_j}{2\left(\Delta\theta\right)^2}\right\}+\omega_{i,j}^{n}\left\{\frac{1}{\Delta t}-\frac{Vi_P\Omega2_j}{\left(\Delta\theta\right)^2}-\frac{Vi_P\Omega4_j}{\left(\Delta w_P\right)^2}\right\}+$$

$$\omega_{i+1,j}^{n}\left\{\frac{-\Omega1_j\left(\psi_{i+1,j+1}^{n}-\psi_{i+1,j-1}^{n}\right)}{16\Delta w_P\Delta\theta}+\frac{Vi_P\Omega2_j}{2\left(\Delta\theta\right)^2}\right\}+$$

$$\omega_{i,j-1}^{n}\left\{\frac{-\Omega1_j\left(\psi_{i+1,j-1}^{n}-\psi_{i-1,j-1}^{n}\right)}{16\Delta w_P\Delta\theta}+\frac{Vi_P\Omega3_j}{2\left(\Delta w_P\right)^2}-\frac{Vi_P\Omega4_j}{4\Delta w_P}\right\}\tag{A.10}$$

In the next equations f is either f or g, depending on the phase P.

$$\Omega1_j=\frac{1}{f'(w_j)(1-\varepsilon)\left(\varepsilon+f(w_j)(1-\varepsilon)\right)}\bigg|_P\tag{A.11}$$

$$\Omega2_j=\frac{1}{\left(\varepsilon+f(w_j)(1-\varepsilon)\right)^2}\bigg|_P\tag{A.12}$$

$$\Omega 3_j = \left( \frac{1}{f'(w_j)(1-\varepsilon)} \right)^2 \Bigg|_P \tag{A.13}$$

$$\Omega 4_j = \frac{1}{f'(w_j)(1-\varepsilon)\big(\varepsilon + f(w_j)(1-\varepsilon)\big)} - \frac{1}{(1-\varepsilon)^2} \frac{f''(w)}{f'(w)^3} \Bigg|_P \tag{A.14}$$

The continuity equation:

$$\omega_{i,j}^{n+1} + \psi_{i,j+1}^{n+1} \left\{ \frac{-\Omega 3_j}{(\Delta w_P)^2} - \frac{\Omega 4_j}{2\Delta w_P} \right\} + \psi_{i-1,j}^{n+1} \left\{ \frac{-\Omega 2_j}{(\Delta\theta)^2} \right\} + \psi_{i,j}^{n+1} \left\{ \frac{2\cdot\Omega 2_j}{(\Delta\theta)^2} + \frac{2\cdot\Omega 3_j}{(\Delta w_P)^2} \right\} +$$

$$\psi_{i+1,j}^{n+1} \left\{ \frac{-\Omega 2_j}{(\Delta\theta)^2} \right\} + \psi_{i,j-1}^{n+1} \left\{ \frac{-\Omega 3_j}{(\Delta w_P)^2} + \frac{\Omega 4_j}{2\Delta w_P} \right\} = 0 \tag{A.15}$$

The convection-diffusion equation:

$$c_{i,j+1}^{n+1} \left\{ \frac{-\Omega 1_j \big(\psi_{i+1,j+1}^{n+1} - \psi_{i-1,j+1}^{n+1}\big)}{16\Delta w_P \Delta\theta} + \frac{-\Omega 1_j \big(\psi_{i+1,j+1}^{n} - \psi_{i-1,j+1}^{n}\big)}{16\Delta w_P \Delta\theta} - \frac{\Omega 3_j}{2Sc_P(\Delta w_P)^2} - \frac{\Omega 4_j}{4Sc_P \Delta w_P} \right\} +$$

$$c_{i-1,j}^{n+1} \left\{ \frac{-\Omega 1_j \big(\psi_{i-1,j+1}^{n+1} - \psi_{i-1,j-1}^{n+1}\big)}{16\Delta w_P \Delta\theta} + \frac{-\Omega 1_j \big(\psi_{i-1,j+1}^{n} - \psi_{i-1,j-1}^{n}\big)}{16\Delta w_P \Delta\theta} - \frac{\Omega 2_j}{2Sc_P(\Delta\theta)^2} \right\} +$$

$$c_{i+1,j}^{n+1} \left\{ \frac{\Omega 1_j \big(\psi_{i+1,j+1}^{n+1} - \psi_{i+1,j-1}^{n+1}\big)}{16\Delta w_P \Delta\theta} + \frac{\Omega 1_j \big(\psi_{i+1,j+1}^{n} - \psi_{i+1,j-1}^{n}\big)}{16\Delta w_P \Delta\theta} - \frac{\Omega 2_j}{2Sc_P(\Delta\theta)^2} \right\} +$$

$$c_{i,j-1}^{n+1} \left\{ \frac{\Omega 1_j \big(\psi_{i+1,j-1}^{n+1} - \psi_{i-1,j-1}^{n+1}\big)}{16\Delta w_P \Delta\theta} + \frac{\Omega 1_j \big(\psi_{i+1,j-1}^{n} - \psi_{i-1,j-1}^{n}\big)}{16\Delta w_P \Delta\theta} - \frac{\Omega 3_j}{2Sc_P(\Delta w_P)^2} + \frac{\Omega 4_j}{4Sc_P \Delta w_P} \right\} +$$

$$c_{i,j}^{n+1} \left\{ \frac{1}{\Delta t} + \frac{\Omega 2_j}{Sc_P(\Delta\theta)^2} + \frac{\Omega 3_j}{Sc_P(\Delta w_P)^2} \right\} + \psi_{i-1,j+1}^{n+1} \left\{ \frac{\Omega 1_j \big(\omega_{i,j+1}^{n} - \omega_{i-1,j}^{n}\big)}{16\Delta w_P \Delta\theta} \right\} +$$

$$\psi_{i+1,j+1}^{n+1} \left\{ \frac{\Omega 1_j \big(\omega_{i+1,j}^{n} - \omega_{i,j+1}^{n}\big)}{16\Delta w_P \Delta\theta} \right\} + \psi_{i-1,j-1}^{n+1} \left\{ \frac{\Omega 1_j \big(\omega_{i-1,j}^{n} - \omega_{i,j-1}^{n}\big)}{16\Delta w_P \Delta\theta} \right\} +$$

$$\psi_{i+1,j-1}^{n+1} \left\{ \frac{\Omega 1_j \big(\omega_{i,j-1}^{n} - \omega_{i+1,j}^{n}\big)}{16\Delta w_P \Delta\theta} \right\} = c_{i-1,j}^{n} \left\{ \frac{\Omega 1_j \big(\psi_{i-1,j+1}^{n} - \psi_{i-1,j-1}^{n}\big)}{16\Delta w_P \Delta\theta} + \frac{\Omega 2_j}{2Sc_P(\Delta\theta)^2} \right\} +$$

$$c_{i,j}^{n} \left\{ \frac{1}{\Delta t} - \frac{\Omega 2_j}{Sc_P(\Delta\theta)^2} - \frac{\Omega 4_j}{Sc_P(\Delta w_P)^2} \right\} + c_{i+1,j}^{n} \left\{ \frac{-\Omega 1_j \big(\psi_{i+1,j+1}^{n} - \psi_{i+1,j-1}^{n}\big)}{16\Delta w_P \Delta\theta} + \frac{\Omega 2_j}{2Sc_P(\Delta\theta)^2} \right\} +$$

$$c_{i,j+1}^{n} \left\{ \frac{\Omega 1_j \big(\psi_{i+1,j+1}^{n} - \psi_{i-1,j+1}^{n}\big)}{16\Delta w_P \Delta\theta} + \frac{\Omega 3_j}{2Sc_P(\Delta w_P)^2} + \frac{\Omega 4_j}{4Sc_P \Delta w_P} \right\} +$$

$$c_{i,j-1}^{n} \left\{ \frac{-\Omega 1_j \big(\psi_{i+1,j-1}^{n} - \psi_{i-1,j-1}^{n}\big)}{16\Delta w_P \Delta\theta} + \frac{\Omega 3_j}{2Sc_P(\Delta w_P)^2} - \frac{\Omega 4_j}{4Sc_P \Delta w_P} \right\} \tag{A.16}$$

## Appendix B

In this appendix, the derivation of the difference formulas for the gas phase vorticity at the interface ($\omega_{i,N_{wL}+1}^{n+1}$) is presented.

*Flat container*

To obtain the required formula for the gas phase vorticity at the interface, the continuity equation (5) has to be combined with the no-slip condition (16). From appendix A, the continuity equation for the liquid phase and the gas phase vorticity are obtained:

$$\omega_{L,i} = \left(\frac{2\eta}{f'(1)(1-\varepsilon)}\right)\frac{\partial^2\psi}{\partial\eta\partial w} + \left(\frac{-1}{\left(f'(1)(1-\varepsilon)\right)^2}\right)\frac{\partial^2\psi}{\partial w^2} + \left(\frac{1}{(1-\varepsilon)^2}\frac{f''(1)}{f'(1)^3}\right)\frac{\partial\psi}{\partial w} \quad (B.1)$$

$$\omega_{G,i} = \left(\frac{2\eta}{g'(1)(1-\varepsilon)}\right)\frac{\partial^2\psi}{\partial\eta\partial w} + \left(\frac{-1}{\left(g'(1)(1-\varepsilon)\right)^2}\right)\frac{\partial^2\psi}{\partial w^2} + \left(\frac{1}{(1-\varepsilon)^2}\frac{g''(1)}{g'(1)^3}\right)\frac{\partial\psi}{\partial w} \quad (B.2)$$

The no-slip condition is expressed by the following equation:

$$\left(\frac{1}{f'(1)(1-\varepsilon)}\right)\frac{\partial\psi}{\partial w}\bigg|_L = \left(\frac{1}{g'(1)(1-\varepsilon)}\right)\frac{\partial\psi}{\partial w}\bigg|_G = h(0) \quad (B.3)$$

$$\left(\frac{1}{f'(1)(1-\varepsilon)}\right)\frac{\partial^2\psi}{\partial\eta\partial w}\bigg|_L = \left(\frac{1}{g'(1)(1-\varepsilon)}\right)\frac{\partial^2\psi}{\partial\eta\partial w}\bigg|_G = h'(0) \quad (B.4)$$

The second derivative of $\psi$ with $w$ in the liquid phase is represented by the next formula, which is derived from Taylor expansion of $\psi(\eta, 1-\Delta w_L)$ and $\psi(\eta, 1-2\Delta w_L)$:

$$\frac{\partial^2\psi}{\partial w^2}\bigg|_L = \frac{4}{\Delta w_L^2}\psi(\eta,1-\Delta w_L) - \frac{1}{2\Delta w_L^2}\psi(\eta,1-2\Delta w_L) + \frac{3}{\Delta w_L}\frac{\partial\psi}{\partial w}\bigg|_L + O(\Delta w_L^2)$$

$$(B.5)$$

When a similar formula for the gas phase is used and substituted in the continuity equation, the following expressions for interface vorticity are obtained:

$$\omega_{L,i} = 2\eta h'(0) + \left(\frac{-1}{\left(f'(1)(1-\varepsilon)\right)^2}\right)\cdot\left(\frac{4\psi(\eta,1-\Delta w_L)}{\Delta w_L^2} - \frac{\psi(\eta,1-2\Delta w_L)}{2\Delta w_L^2}\right) +$$

$$+ h(0)\left(\frac{-3}{\Delta w_L f'(1)(1-\varepsilon)} + \frac{1}{(1-\varepsilon)}\frac{f''(1)}{f'(1)^2}\right) \quad (B.6)$$

$$\omega_{G,i} = 2\eta h'(0) + \left(\frac{-1}{\left(g'(1)(1-\varepsilon)\right)^2}\right) \cdot \left(\frac{4\psi\left(\eta,1+\Delta w_G\right)}{\Delta w_G^2} - \frac{\psi\left(\eta,1+2\Delta w_G\right)}{2\Delta w_G^2}\right) +$$

$$-h(0)\left(\frac{-3}{\Delta w_G g'(1)(1-\varepsilon)} - \frac{1}{(1-\varepsilon)}\frac{g''(1)}{g'(1)^2}\right) \qquad (B.7)$$

It is possible to eliminate h(0) with a linear combination of the final equations for vorticity in the liquid and the gas phase. For the mixed derivative h'(0), a second order approximation is used, which results in $(j = N_{wL+1})$:

$$h'(0) = \left(\frac{1}{f'(1)(1-\varepsilon)}\right)\left(\frac{-4\psi_{i+1,j-2}^{n+1} + \psi_{i+1,j-3}^{n+1} + 4\psi_{i-1,j-2}^{n+1} - \psi_{i-1,j-3}^{n+1}}{4\Delta w_L \Delta\eta}\right) \qquad (B.8)$$

The final formula for the gas phase vorticity at the interface then reads:

$i = 1,.., N_\eta\text{-}1; \; j = N_{wL+1}$

$$\frac{\omega_{i,j-1}^{n+1}}{X_L} + \frac{\omega_{i,j}^{n+1}}{X_G} = \left(\frac{2\eta_i\left(\dfrac{1}{X_L} + \dfrac{1}{X_G}\right)}{f'(1)(1-\varepsilon)}\right)\left(\frac{-4\psi_{i+1,j-2}^{n+1} + \psi_{i+1,j-3}^{n+1} + 4\psi_{i-1,j-2}^{n+1} - \psi_{i-1,j-3}^{n+1}}{4\Delta w_L \Delta\eta}\right) +$$

$$\left(\frac{-1}{\left(f'(1)(1-\varepsilon)\right)^2 X_L}\right) \cdot \left(\frac{4}{\Delta w_L^2}\psi_{i,j-2}^{n+1} - \frac{1}{2\Delta w_L^2}\psi_{i,j-3}^{n+1}\right) +$$

$$\left(\frac{-1}{\left(g'(1)(1-\varepsilon)\right)^2 X_G}\right) \cdot \left(\frac{4}{\Delta w_G^2}\psi_{i,j+1}^{n+1} - \frac{1}{2\Delta w_G^2}\psi_{i,j+2}^{n+1}\right) \qquad (B.9)$$

In this equation, $X_L$ and $X_G$ are:

$$X_L = \frac{-3}{\Delta w_L f'(1)(1-\varepsilon)} + \frac{f''(1)}{(1-\varepsilon)f'(1)^2} \qquad (B.10)$$

$$X_G = \frac{-3}{\Delta w_G g'(1)(1-\varepsilon)} - \frac{g''(1)}{(1-\varepsilon)g'(1)^2} \qquad (B.11)$$

*Convex container*

After an analogous derivation, the following formula for the gas phase vorticity is obtained:

$i = 1,..., N_\theta-1; j = N_{wL+1}$

$$\frac{\omega_{i,j-1}^{n+1}}{X_L} + \frac{\omega_{i,j}^{n+1}}{X_G} = \left(\frac{1}{\left(f'(1)(1-\varepsilon)\right)^2 X_L}\right) \cdot \left(\frac{4}{\Delta w_L^2}\psi_{i,j-2}^{n+1} - \frac{1}{2\Delta w_L^2}\psi_{i,j-3}^{n+1}\right) +$$

$$\left(\frac{1}{\left(g'(1)(1-\varepsilon)\right)^2 X_G}\right) \cdot \left(\frac{4}{\Delta w_G^2}\psi_{i,j+1}^{n+1} - \frac{1}{2\Delta w_G^2}\psi_{i,j+2}^{n+1}\right) \qquad (B.12)$$

In this equation, $X_L$ and $X_G$ are:

$$X_L = 1 + \frac{3}{\Delta w_L f'(1)(1-\varepsilon)} - \frac{f''(1)}{(1-\varepsilon)f'(1)^2} \qquad (B.13)$$

$$X_G = -1 + \frac{3}{\Delta w_G g'(1)(1-\varepsilon)} + \frac{g''(1)}{(1-\varepsilon)g'(1)^2} \qquad (B.14)$$